Author Contributions:
Conceptualization: Yuanhao Fang, Guo-Yue Niu
Formal analysis: Xue-Yan Zhang, Guo-Yue Niu
Funding acquisition: Xubin Zeng
Investigation: Xue-Yan Zhang
Methodology: Xue-Yan Zhang, Guo-Yue Niu
Project Administration: Xubin Zeng
Resources: Guo-Yue Niu

Impacts of Topography-Driven Water Redistribution on Terrestrial Water Storage Change in California Through Ecosystem Responses

Xue-Yan Zhang[1] , Yuanhao Fang[1,2] , Guo-Yue Niu[1] , Peter A. Troch[1,3] , Bo Guo[1] , L. Ruby Leung[4] , Michael A. Brunke[1], Patrick Broxton[5] , and Xubin Zeng[1]

[1]Department of Hydrology and Atmospheric Sciences, The University of Arizona, Tucson, AZ, USA, [2]College of Hydrology and Water Resources, Hohai University, Nanjing, China, [3]Biosphere 2, University of Arizona, Tucson, AZ, USA, [4]Atmospheric Sciences and Global Change Division, Pacific Northwest National Laboratory, Richland, WA, USA, [5]School of Natural Resources and the Environment, University of Arizona, Tucson, AZ, USA

Abstract Lateral subsurface flow plays an essential role in sustaining the terrestrial ecosystem, but it is not explicitly represented in most Earth System Models. In this study, we implemented an explicit lateral saturated flow model into the E3SM land model (ELM). The model explicitly describes lateral flow in the saturated zone by representing, for each model grid, an idealized hillslope consisting of five hydrologically connected soil columns. We conducted three model experiments driven by 0.125° atmospheric forcing data during 1980–2015 over California using models of the default ELM, a modified version of ELM to enhance infiltration, and the model with the lateral saturated flow model. The simulated runoff, evapotranspiration, and terrestrial water storage anomaly (TWSA) from the three simulations were evaluated against available observations, and the model explicitly representing lateral flow performs best. The new model produces greater gridcell-averaged evapotranspiration especially over the mountainous regions with moderate relief and seasonally dry climates. Most importantly, it improves the modeled seasonal variations, interannual variabilities, and the recent decadal decline of TWSA. Many of these improvements can be attributed to the enhanced ecosystem resilience to droughts as demonstrated by transpiration increases caused by lateral flow. Model sensitivity experiments suggest that subsurface runoff is most sensitive to the ratio between horizontal and vertical saturated hydraulic conductivity, followed by hillslope planforms (convergent, divergent, and uniform), number of columns, and lower boundary conditions. Future work should effectively characterize hillslopes in global models and explore the long-term influences of lateral water movement on modeled biogeochemical cycle.

Plain Language Summary In this study, we implemented a lateral saturated flow scheme into the Energy Exascale Earth System Model's land model (ELM) to explicitly represent lateral groundwater movement. We applied our newly developed model over California and found better model performance against the original and a revised version of ELM through the explicit yet simplified representation of lateral flow along hillslopes. Most importantly, our new model does a better job at reproducing the seasonal variations, interannual variabilities, and a declining trend of terrestrial water storage anomaly in California. Given the intensified coupling among water, energy, and carbon cycles associated with climate change, our study highlights the need to implement lateral flow in Earth System Models for better climate projections.

1. Introduction

The western United States (US) has been experiencing more severe, frequent, and longer droughts characterized by anomalously low precipitation and exacerbated by high temperatures due to anthropogenic warming (Luo et al., 2017; Ullrich et al., 2018; Williams et al., 2020). Since 2000, the western US may have been in the second driest megadrought in the past 1,200 years as indicated by tree-ring reconstructions of summer soil moisture (Williams et al., 2020). This megadrought is likely associated with cooler-than-normal sea-surface temperature (SST) in the eastern tropical Pacific (Cook et al., 2018), warmer-than-normal SSTs in the north Atlantic (Feng et al., 2011), and poleward expansion of the subtropical ridge (Ault et al., 2016; Ting et al., 2018), leading to less precipitation in winter. In addition, the warming-induced increases in evaporative demand in summer and associated reductions in runoff and soil moisture (Ault et al., 2016; Ting et al., 2018) contribute substantially to the drought severity (Williams et al., 2020). Land surface feedbacks may amplify and perpetuate droughts that

Software: Xue-Yan Zhang, Yuanhao Fang, Bo Guo
Supervision: Guo-Yue Niu, Xubin Zeng
Validation: Xue-Yan Zhang
Writing – original draft: Xue-Yan Zhang
Writing – review & editing: Xue-Yan Zhang, Guo-Yue Niu, Peter A. Troch, Bo Guo, L. Ruby Leung, Michael A. Brunke, Patrick Broxton, Xubin Zeng

are triggered by SST anomalies (Hong & Kalnay, 2000; Schubert et al., 2004; Xue & Shukla, 1993). In other words, land surface states and land-atmosphere interactions are of great importance to drought predictabilities in the mid-latitude land regions (Koster, Suarez, & Heiser, 2000). However, current climate models or Earth System Models (ESMs) still have deficiencies in representing various key land surface processes. For example, ESMs substantially underestimate evapotranspiration (ET) especially during droughts (Dong et al., 2022; Zhao et al., 2022) due to model deficiencies in representing key hydrological processes such as plant and soil hydraulics, snow sublimation, and topography-driven lateral flow. In this study, we focus on the impacts of topography-driven lateral subsurface flow on terrestrial water storage change over California, a region that has been experiencing a megadrought during the past decades.

Topography-driven lateral subsurface flow modulates water, energy, and biogeochemical (e.g., carbon) fluxes through water redistribution and land-atmosphere interactions differently depending on regional climates and surface conditions (Chang et al., 2018; Fan et al., 2019; Maxwell & Condon, 2016; Maxwell & Kollet, 2008; Shrestha et al., 2015). Lateral subsurface flow increases the ratio of transpiration to evapotranspiration or T/ET (Chang et al., 2018; Maxwell & Condon, 2016), improves plant water use efficiency (Chang et al., 2018) and photosynthesis (Govind et al., 2011), and thus enhances ecosystem drought resilience (Chang et al., 2018; Hoylman et al., 2018; Maxwell & Kollet, 2008; Tai et al., 2021). For example, using multiple remote sensing products, Tai et al. (2020) observed increasing vegetation productivity and less precipitation sensitivity with greater topography convergence in a forested watershed in the Rocky Mountains. The strong coupling between terrestrial water and carbon cycles also produces much greater modeled soil carbon concentrations in the valleys than the hilltops globally due to hillslope flow convergence (Subin et al., 2014). The changes of land surface heat fluxes associated with lateral subsurface flow can feed back to the atmosphere through land-atmosphere interactions, affect the atmospheric boundary layer development, and thus change the lower atmospheric variables, such as cooling air temperatures and enhancing precipitation (Arboleda Obando et al., 2022; Maxwell et al., 2007). Barlage et al. (2021) demonstrated that a high-resolution representation of the intercell lateral groundwater flow substantially reduces summer warm-and-dry bias in the central US. It should be noted that the modeled impacts of lateral subsurface flow on soil moisture and related ecohydrological variables are scale-dependent and become more prominent at finer resolutions (Barlage et al., 2021; Ji et al., 2017; Krakauer et al., 2014; Shrestha et al., 2015, 2018). The explicit implementation of lateral subsurface flow to ESMs is essential to achieve better future climate projections, especially given the increased prevalence of droughts.

ESMs are important tools to understand and predict global climate changes. Despite the importance of topography-driven lateral subsurface flow, most ESMs operate on grid box sizes of around 100 km and only represent one-dimensional (1-D) vertical flow through the soil matrix (Fan et al., 2019; Hazenberg et al., 2016; Subin et al., 2014; Swenson et al., 2019). Early land models in ESMs represented land surface hydrology as a simple bucket and highly parameterized heterogeneous land surface characteristics and associated lateral subsurface flow (Schaake et al., 1996; Yang & Dickinson, 1996). Recognizing the importance of lateral subsurface flow, land models started to implicitly represent lateral subsurface flow by considering static subgrid variabilities, such as soil moisture or water table depth (Warrach et al., 2002). For example, the TOPMODEL concept used in many land models uses a topographic wetness index (or wetness index) to represent topographic effects on the static subgrid heterogeneity of soil moisture and thus partially captures hillslope hydrologic responses (Beven & Kirkby, 1979; Chen & Kumar, 2001; Famiglietti & Wood, 1991, 1994; Koster, Suarez, Ducharne, et al., 2000; Niu et al., 2005; Stieglitz et al., 1997; Yang & Niu, 2003). Despite its simplicity and efficiency, TOPMODEL cannot explicitly describe dynamic subsurface flow with small-scale hydrological variations over complex terrain. In addition, the next-generation hyper-resolution ESMs require sophisticated and realistic hillslope-scale hydrology representations.

Numerous studies have begun to explicitly represent lateral subsurface flow movement in ESMs with various complexities. Many studies have been conducted to couple three-dimensional (3-D) groundwater models with land surface models that solves 3-D variably saturated Richards equation (Bisht et al., 2017; Kollet & Maxwell, 2008; Kuffour et al., 2020; Maxwell & Miller, 2005; Niu et al., 2014; O'neill et al., 2021; Tian et al., 2012; York et al., 2002). To reduce the computational burden, quasi-3D schemes were developed to represent intercell (2-D) lateral saturated subsurface flow and vertical soil water flow separately (Fan et al., 2007; Felfelani et al., 2021; Shen et al., 2013; Xie et al., 2012; Zeng, Xie, et al., 2018; Zeng et al., 2016). Recently, Qiu et al. (2023) incorporated intercell lateral unsaturated and saturated flow in a land model. But the high computational cost, the data volume, and complexity required by these 3-D and quasi-3D approaches constrains their uses for global

applications. An alternative practical method is to couple the 1-D Richards equation with intracell (1-D) lateral flow along representative hillslopes (Chaney et al., 2016, 2018, 2021; Hazenberg et al., 2015; Subin et al., 2014; Swenson et al., 2019). A hybrid-3D hillslope hydrological model (H3D) developed by Hazenberg et al. (2015) can simulate hillslope hydrology responses comparable to the complex 3D physically-based model, CATchment HYdrology CATHY (Paniconi et al., 2003; Paniconi & Putti, 1994; Paniconi & Wood, 1993) at much higher computational efficiency saving computational time by up to three orders of magnitude (Hazenberg et al., 2016). H3D couples a 1-D vertical flow model with a pseudo-2D lateral flow model represented by the hillslope-storage Boussinesq (hsB) equation. The 1-D hsB equation can reproduce the 2-D lateral saturated subsurface flow at the hillslope scale (Hilberts et al., 2004; Paniconi et al., 2003; Troch et al., 2003). This computationally efficient H3D provides a promising way to incorporating hillslope-scale hydrology to ESMs.

In this work, we coupled the hsB equation of H3D (Hazenberg et al., 2015; Troch et al., 2003) to the land model (ELM) of the Energy Exascale Earth System Model (E3SM) that, like many other ESMs, does not represent lateral subsurface flow movement. We tested our new model (ELM$_{H3D}$) over California, which has experienced increasingly severe droughts and heatwaves. We also quantified the influences of explicit lateral flow on modeled hydrological fluxes and states that are important to drought assessment and predictions. Lastly, we performed multiple sensitivity experiments to better understand the sensitivity of subsurface runoff changes to the hillslope parameters.

2. Methods

2.1. Data

2.1.1. Climate Forcings

The meteorological data used to drive all model experiments is from the National Land Data Assimilation System Phase 2 (NLDAS-2) for 1980–2015 (Xia et al., 2012). This data set includes hourly 0.125° precipitation, short-wave and longwave downward radiation, wind speed, specific humidity, surface air temperature and pressure covering the contiguous United States (CONUS). The non-precipitation forcing data of NLDAS-2 is derived by spatially and temporally disaggregating the analysis fields of the NCEP North American Regional Reanalysis (NARR) with vertical adjustment to account for terrain height differences between NLDAS-2 and NARR (Xia et al., 2012). The topographically adjusted Climate Prediction Center (CPC) CONUS daily gauge data is temporally disaggregated into hourly NLDAS-2 precipitation (Xia et al., 2012). The hourly temporal disaggregation weights are from NCEP hourly Stage II Doppler radar precipitation data, half-hourly CPC-Morphing technique data (Joyce et al., 2004), and 3-hourly NARR data.

2.1.2. Model Validation Data

To calibrate and validate model performances, we used monthly observed runoff, snow water equivalent (SWE), ET, and terrestrial water storage anomaly (TWSA). We obtained the observed monthly runoff from the US Geological Survey (USGS) for the two-digital hydrological unit code (HUC) 18, which covers all of California. This runoff data set is generated by incorporating streamflow observations, the drainage basins of stream-flow gages, and HUC boundaries (Brakebill et al., 2011). We used 4-km daily SWE from the University of Arizona (UA) to validate modeled SWE from 1982 to 2015. The UA SWE data set is derived by assimilating ground-based snow observations from National Resource Conservation Service Snow Telemetry and the National Weather Service Cooperative Observer networks and gridded precipitation and temperature data from the Parameter-elevation Regressions on Independent Slopes Model (Broxton et al., 2016; Dawson et al., 2017; Zeng, Broxton, & Dawson, 2018). We also used the 0.5° monthly FLUXNET Model Tree Ensembles (MTE) gridded ET data set to assess modeled ET during 1982–2011. The FLUXNET MTE data is generated by upscaling FLUXNET in situ observations of water, carbon, and energy fluxes with the MTE machine learning method to the global scale, which has been used by various studies (Jung et al., 2011; Ma et al., 2017; Zhang et al., 2022). The UA SWE and FLUXNET MTE products were bilinearly interpolated to a spatial resolution of 0.125° to be consistent with our model outputs. We used 1° monthly Gravity Recovery and Climate Experiment (GRACE) Release 05 Level-3 TWSA products during 2003–2015 derived from spherical harmonics (SH) solutions from the University of Texas Center for Space Research (CSR), the Jet Propulsion Laboratory (JPL), and the GeoForschungsZentrum (GFZ), because the gain factor for Release 06 SH products are not accessible currently. We multiplied three GRACE SH products with their gain factors to compensate for the

signal leakage issues (Landerer & Swenson, 2012). We also used monthly half-degree GRACE/GRACE-FO Release 06 (RL06) Level-3 mass concentration solutions (Mascons) from JPL and the NASA Goddard Space Flight Center (GSFC) and 0.25° RL06 Mascons from CSR. Then, we averaged these three SH (GRACE$_{SH}$) and Mascons (GRACE$_{Mascons}$) products to reduce the noise associated with different solutions, respectively (Sakumura et al., 2014).

2.2. Models and Experiments

2.2.1. The ELM Model

The ELM version 1 of E3SM is developed based on the Community Land Model version 4.5 (CLM 4.5) with new parameterizations of soil hydrology and biogeochemistry (Leung et al., 2020). The subgrid heterogeneity of each grid cell is represented through a hierarchy system of three subgrid levels including five land units, soil/snow columns, and up to 16 plant functional types (PFTs). The five land units include glacier, lake, urban, natural vegetation, and crops. Each grid cell has one soil/snow column on the vegetated land unit as well as additional columns for other land units, as applicable. Land surface data with a spatial resolution of 0.125° over the NLDAS domain is generated using the tool provided by ELM. This surface data set primarily describes the fractions of land units (e.g., lake and vegetation), soil properties, characteristics of each vegetation type, topography, and others in a model grid. The subgrid spatial distribution of PFTs is derived from the Moderate Resolution Imaging Spectroradiometer and Advanced Very High Resolution Radiometer satellite observations (Lawrence & Chase, 2007) and kept static throughout the entire model experiments. The variable soil thickness is represented by the 30 arcsec (∼1 km) global data set of bedrock depth (Pelletier et al., 2016). The default ELM has only one soil column in a model grid, while for the hillslope model the soil column is divided into several soil columns along one representative hillslope. Each of the soil columns shares the same land surface properties (e.g., PFTs, soil thickness, and slope angle) of the model grid.

In this study, we mainly focus on soil hydrology and runoff generation. Total runoff is the sum of saturation-excess surface runoff (Q_{over}; mm/s), subsurface runoff (Q_{drai}; mm/s), infiltration-excess surface runoff (more exactly, runoff of surface ponded water) (Q_{h2osfc}; mm/s), and runoff from glaciers and lakes (Q_{rgwl}; mm/s). Q_{rgwl} is the imbalance term in the water budget of glaciers and lakes, which may be negative. Two options of runoff schemes, VIC (Variable Infiltration Capacity) and the TOPMODEL-based (a topography-based hydrological model), are provided in ELM. We chose the TOPMODEL scheme in the default and modified model experiments (see Section 2.2.3). Surface (Q_{over}) and subsurface (Q_{drai}) runoff are parameterized based on the simple TOPMODEL (SIMTOP) concept (Niu et al., 2005). But subsurface runoff (or groundwater discharge) is largely reduced for frozen soils by multiplying an ice impedance factor (Θ_{ice}) in ELM (Equation 1). The frozen soil permeability (Equation 3) is also remarkably reduced by multiplying Θ_{ice} in the default ELM option of soil hydraulic property scheme (Swenson et al., 2012). The detailed equations for other runoff components were included in Supporting Information S1 (Text S1).

$$Q_{drai} = \Theta_{ice} \times q_{drai,max} \times e^{-f_{sub} \times z_{wt}} \tag{1}$$

$$\Theta_{ice} = 10^{-\Omega \times \frac{\theta_{ice}}{\theta_{sat}}} \tag{2}$$

$$k_i = \begin{cases} \Theta_{ice} \, k_{sat,i} \left\{ \dfrac{0.5 * (\theta_i + \theta_{i+1})}{0.5 * (\theta_{sat,i} + \theta_{sat,i+1})} \right\}^{2b_i+3} & (1 \le i \le N_{levsoi} - 1) \\ \Theta_{ice} \, k_{sat,i} \left\{ \dfrac{\theta_i}{\theta_{sat,i}} \right\}^{2b_i+3} & (i = N_{levsoi}) \end{cases} \tag{3}$$

where $\frac{\theta_{ice}}{\theta_{sat}}$ is the ice fraction for the soils under the groundwater table; Ω is an adjustable parameter with a default value of 6; $q_{drai,max}$ is the maximum subsurface runoff (mm/s); $q_{drai,max} = 10 \sin(\alpha)$; α is the gridcell mean topographic slope angle in radians; f_{sub} is a decay factor for subsurface runoff with a default value of 2.5; z_{wt} is the water table depth (m); k_i and $k_{sat,i}$ are the actual and saturated soil hydraulic conductivity at soil layer i (mm/s), respectively; θ_i and $\theta_{sat,i}$ are the volumetric soil liquid water and porosity at soil layer i; b_i is the Clapp-Hornberger pore size distribution index determined by soil texture at soil layer i, and N_{levsoi} is the number of soil layers.

2.2.2. Implementing the Representative Hillslope Lateral Flow Model Into ELM

To properly represent hillslope hydrological responses at a low computational cost, we replaced the SIMTOP subsurface runoff scheme (Equation 1) with the hsB equation of H3D (Equation 4). The hsB equation is derived by combining the Boussinesq equation with the hillslope width function (Hazenberg et al., 2015; Troch et al., 2003) based on the assumption that the average water table depth as a function of distance from the seepage face is constant (Fan & Bras, 1998).

$$f \frac{\partial h}{\partial t} = \frac{1}{w} \frac{\partial}{\partial x} \left(w \, k_l(h) \, h \left(\sin(\alpha) + \frac{\partial h}{\partial x} \cos(\alpha) \right) \right) + \cos(\alpha) R_{sat} \tag{4}$$

where f is the drainable porosity, h (m) is the height of the saturated zone perpendicular to the hillslope bedrock with a slope angle α, w (m) is the width of the hillslope at a given distance x (m) from the outflow point, $k_l(h)$ (m/s) is the lateral saturated hydraulic conductivity at height h. R_{sat} is the recharge rate between the unsaturated and saturated zones (m/s). The iterative implicit finite difference method is used to numerically solve the hsB equation with an iteration criterion of $h_j^{t,s+1} - h_j^{t,s} < \delta_{th} = 0.1$ m (Hazenberg et al., 2015).

$$\begin{aligned}
f \left(h_j^{t,s+1} - h_j^{t-1} \right) &= \frac{\Delta T \, \sin(\alpha)}{w_j \Delta x_j} \left(w_{j+0.5} \, k_{l_{j+0.5}}^{t,s} \, h_{j+0.5}^{t,s} - w_{j-0.5} \, k_{l_{j-0.5}}^{t,s} \, h_{j-0.5}^{t,s} \right) \\
&+ \frac{\Delta T \, \cos(\alpha)}{w_j \Delta x_j} \left(\frac{w_{j+0.5} \, k_{l_{j+0.5}}^{t,s} \, h_{j+0.5}^{t,s}}{\Delta x_{U_j}} \left(h_{j+1}^{t,s+1} - h_j^{t,s+1} \right) \right. \\
&\left. - \frac{w_{j-0.5} \, k_{l_{j-0.5}}^{t,s} \, h_{j-0.5}^{t,s}}{\Delta x_{L_j}} \left(h_j^{t,s+1} - h_{j-1}^{t,s+1} \right) \right) + \Delta T \, \cos(\alpha) \, R_{sat_j}^t
\end{aligned} \tag{5}$$

where ΔT (seconds) is the time step, j is the lateral node number, t is the time of interest, and s is the iteration step. Δx_{U_j} and Δx_{L_j} is the distance (m) relative to the center of upper $j + 1$ and lower $j - 1$ node. w_j is the width on the center of node j. $j - 0.5$ and $j + 0.5$ represent the lower and upper bounds of node j.

For the upper lateral boundary, zero lateral flux is assumed flowing into the top of the hillslope. Therefore, the numerical equation for the upper node N is:

$$\begin{aligned}
f \left(h_N^{t,s+1} - h_N^{t-1} \right) &= -\frac{\Delta T \, \sin(\alpha)}{w_N \Delta x_N} \left(w_{N-0.5} \, k_{l_{N-0.5}}^{t,s} \, h_{N-0.5}^{t,s} \right) \\
&- \frac{\Delta T \, \cos(\alpha)}{w_N \Delta x_N} \left(\frac{w_{N-0.5} \, k_{l_{N-0.5}}^{t,s} \, h_{N-0.5}^{t,s}}{\Delta x_{L_N}} \left(h_N^{t,s+1} - h_{N-1}^{t,s+1} \right) \right) \\
&+ \Delta T \, \cos(\alpha) R_{sat_N}^t
\end{aligned} \tag{6}$$

For the lower lateral boundary at the seepage face of the hillslope, a kinematic wave approximation is applied ($\frac{\partial h}{\partial x} = 0$, Equation 7). We further developed an extreme seepage face boundary condition in this study (See Appendix A). Equations 5–7 result in a tridiagonal matrix of $(N + 1)$ equations at the iteration step $s + 1$.

$$\begin{aligned}
f \left(h_0^{t,s+1} - h_0^{t-1} \right) &= \frac{\Delta T \, \sin(\alpha)}{w_0 \Delta x_0} \left(w_{0.5} \, k_{l_{0.5}}^{t,s} \, h_{0.5}^{t,s} \right) \\
&+ \frac{\Delta T \, \cos(\alpha)}{w_0 \Delta x_0} \left(\frac{w_{0.5} \, k_{l_{0.5}}^{t,s} \, h_{0.5}^{t,s}}{\Delta x_{U_0}} \left(h_1^{t,s+1} - h_0^{t,s+1} \right) \right) + \Delta T \, \cos(\alpha) \, R_{sat_0}^t
\end{aligned} \tag{7}$$

To numerically implement the hsB equation in the ELM model, we divided the soil column into a series of equal-length (in the x direction along the hillslope), laterally connected soil columns to form a hillslope (Figure 1). Each gridcell has a single representative hillslope for the vegetated land unit. The lowest soil column is treated as the lowland directly exchanging water fluxes with the river channel. Since we applied the kinematic boundary condition to the lowland, we did not explicitly account for dynamic water exchanges between lowlands and river channels. The height of the saturated zone (h) is computed by subtracting the water table depth from the bedrock depth. The term $(\cos(\alpha) R_{sat})$ is removed in the hsB code implementation in ELM because aquifer mass changes due to groundwater recharge have been represented after solving the 1-D Richards equation in ELM. We set the iteration standard of $\delta_{th} < 0.1$ mm. The timestep for the hsB solver (Δt_{fine}) in ELM is initially set as the temporal resolution of the atmospheric forcing, dt (e.g.,
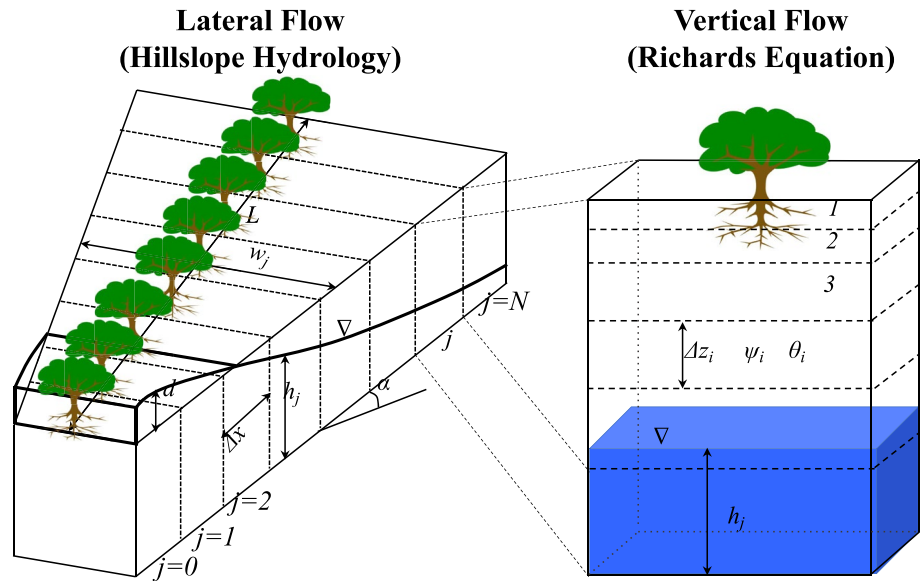
Figure 1. Numerical implementation of a hybrid-3D hillslope hydrological model. (left) the spatial view of a hillslope with a total length L consisting of N vertical soil columns with equal length (Δx) on the top of bedrock with a topographic slope (α). W represents the width of hillslope at a distance from the lower border of the lowest column (column 0). j represents the index of hillslope column center. The land surface properties (e.g., bedrock depth and vegetation distribution) and forcing inputs on each column are the same. d represents the depth of overland flow. (right) the vertical dimension of a hillslope column. The vertical flow travels through multiple soil layers with varying soil layer thickness (Δz_i) and water conditions (θ_i, ψ_i) on top of the impermeable bedrock with zero bottom flux, which is solved by the θ-based form of the Richards equation (Zeng & Decker, 2009). i represents the index of vertical soil layers. h is the height of saturation zone, and ∇ is water table. VSFM is the acronym of vertical soil flow model.

3,600 s in this study). If the solver cannot converge within 20 iterations, Δt_{fine} is reduced to half of the previous Δt_{fine}, returning the previous iteration with the updated smaller time step. The model would stop if the hsB solver cannot converge with the smallest $\Delta t_{fine} = 10$ s. We used an operator splitting approach to update the soil water state through two steps. First, we solved the 1-D vertical flow within the soil column represented by the mass-based form of the Richards equation with zero bottom flux into the bedrock. Second, soil water within the saturated zone is updated due to lateral flow (subsurface runoff) that is controlled by total hydraulic gradients. The gridcell-averaged subsurface runoff is the sum of lateral flows from each soil column in the grid cell weighted by their own hillslope area, instead of the original SIMTOP subsurface runoff scheme (Equation 1).

In this study, each hillslope is discretized into five soil columns (i.e., node 0–4) with a total length of 500 m (100 m for each column). Three theoretical hillslope width functions are used to represent convergent, divergent, and uniform hillslope planforms (Equations 8–10). The hillslope width function computes the width for the upper ($w_{j+0.5}$) and lower ($w_{j-0.5}$) interfaces and the center (w_j) of each node. Then, the width of each node for the hillslope is recomputed by matching the total hillslope area to the total area of the vegetated land unit in each gridcell. f is treated as the specific yield at the top of the saturated zone. α is directly obtained from the ELM land surface input data. We parameterized $k_l(h)$ by multiplying the vertical saturated hydraulic conductivity at the top of the saturated zone with an anisotropic factor (ζ). To simplify the downscaling process, the land surface properties and forcing inputs for all hillslope soil columns in each gridcell, such as soil properties, bedrock depth, and distributions of PFTs, are identical to the single soil column in each gridcell of ELM.

$$w_{j+0.5} = \exp\left(hs * \frac{j+1}{N+1} \right); w_{-0.5} = 1.0 \tag{8}$$

$$w_{j+0.5} = \exp\left(-hs * \frac{j+1}{N+1} \right); w_{-0.5} = 1.0 \tag{9}$$

$$w_{-0.5} = w_{j+0.5} = 1.0 \tag{10}$$

Table 1
The Parameterization Scheme and Code Changes in $ELM_{default}$*,* ELM_{mod}*, and* ELM_{H3D}

Model	Initial conditions	Parameterization options	Code
$ELM_{default}$	$\theta_i = 0.15$	Scheme of soil hydraulic properties = Swenson et al. (2012)	$max_{fpi} = 0.25$
	$z_{wt} = zibed - 0.01$		$k = 0.1$, $ssi = 0.033$
			$f_c = 0.4$, $\mu = 0.14$
			$f_{over} = 0.5$, $f_{sub} = 2.5$
		Soil stress method = Lee and Pielke (1992)	$beddep = \max(0.2, aveDTB)$
		Precipitation partitioning = Lawrence et al. (2019)	$q_{in,max} = (1 - f_{sat}) * min(10^{(-\Omega*(icefrac(1:3)))*hksat(1:3)})$
			$organic3d$ (Read from surface data)
ELM_{mod}	$\theta_i = \begin{cases} 0.6 * \theta_{sat,i} \ (i < 5) \\ \\ \theta_{sat,i} \ (else) \end{cases}$	Scheme of soil hydraulic properties = Niu and Yang (2006)	$max_{fpi} = 0.15$
			$k = 0.5$, $ssi = 0.08$
			$f_c = 0.8$, $\mu = 2.0$
			$f_{over} = 2$, $f_{sub} = 2$
	$z_{wt} = \begin{cases} zibed * 0.3 \ (nlevbed > 6) \\ \\ zibed * 0.5 \ (else) \end{cases}$	Soil stress method = Sakaguchi and Zeng (2009)	$beddep = max(2, aveDTB)$
			$q_{in,max} = (1 - f_{sat}) * min(hksat(1:3))$
		Precipitation partitioning = Jordan (1991)	$organic3d = 0$
ELM_{H3D}	Same as ELM_{mod}	Same as ELM_{mod}	Same as ELM_{mod}
			convergent hillslope (length: 500 m)
			anisotropic ratio (ζ) = 10

Note. θ_i is volumetric soil water content, $\theta_{sat,i}$ is soil porosity of the i th soil layer, and i is the index of soil layers. z_{wt} is water table depth (m), $zibed$ is the depth to bedrock (m), and $nlevbed$ is the number of vertical soil layers. max_{fpi} is the maximum canopy interception fraction. k is the shape factor for snow accumulation in the snow cover fraction computation. ssi is the irreducible water saturation of snow. f_c is a global constant threshold beyond which local surface water bodies within a grid cell are connected and runs off. μ is a global constant scaling parameter in the computation of interconnected surface water fraction. f_{over} and f_{sub} are decay factors for surface and subsurface Runoff, respectively. $beddep$ is the bedrock depth, and $aveDTB$ is the surface input of bedrock depth (m). $q_{in,max}$ is the maximum infiltration capacity (mm/s). f_{sat} is the saturated fraction of a gridcell. Ω is a soil ice impedance parameter. $icefrac$ is the volumetric soil ice fraction. $hksat$ is saturated soil hydraulic conductivity (mm/s). $organic3d$ is the soil organic matter fraction. max and min are the maximum and minimum functions, and 1:3 represents soil layers 1–3 from the top.

where N is the number of soil columns in one representative hillslope, hs is the total hillslope length (m), j represents the node number spanning from 0 (valley) to N (hilltop), and w_j is half of the sum of $w_{j-0.5}$ and $w_{j+0.5}$.

2.2.3. Model Experiments

We conducted three experiments: (a) ELM with variable bedrock depth ($ELM_{default}$); (b) ELM_{mod} that is based on $ELM_{default}$ but with multiple code modifications and alternative parameterization options of soil hydraulic properties to enhance infiltration amounts; and (c) ELM_{H3D} that is based on ELM_{mod} but explicitly represents subsurface runoff along convergent hillslopes through the hsB equation (Table 1). $ELM_{default}$ is found to be deficient in water infiltration into the soil, leading to minimal (and unrealistic) dry summer baseflow over California (as discussed in Section 3). To reduce these deficiencies, we made several major revisions in ELM_{mod} as follows (also see Table 1) based on our modeling experience and manual calibrations:

1. To reduce saturated-excess runoff and thus increase infiltration, we modified both the decay factor of SIMTOP surface ($f_{over} = 0.5$) and subsurface runoff ($f_{sub} = 2.5$) to 2 as Niu et al. (2005) suggested; $f_{over} = 0.5$ generally produces too much saturation-excess runoff in desert regions.
2. We changed f_c (0.4) and μ (0.14) to 0.8 and 2.0 and increased the maximum infiltration rates ($q_{in,max}$), respectively, to reduce infiltration-excess runoff and thus increase water fluxes to deeper soil layers.
3. For frozen soils, we used a scheme from Niu and Yang (2006) that considers fractional permeable area in a model grid and computes the soil hydraulic properties based on total soil moisture rather than soil liquid
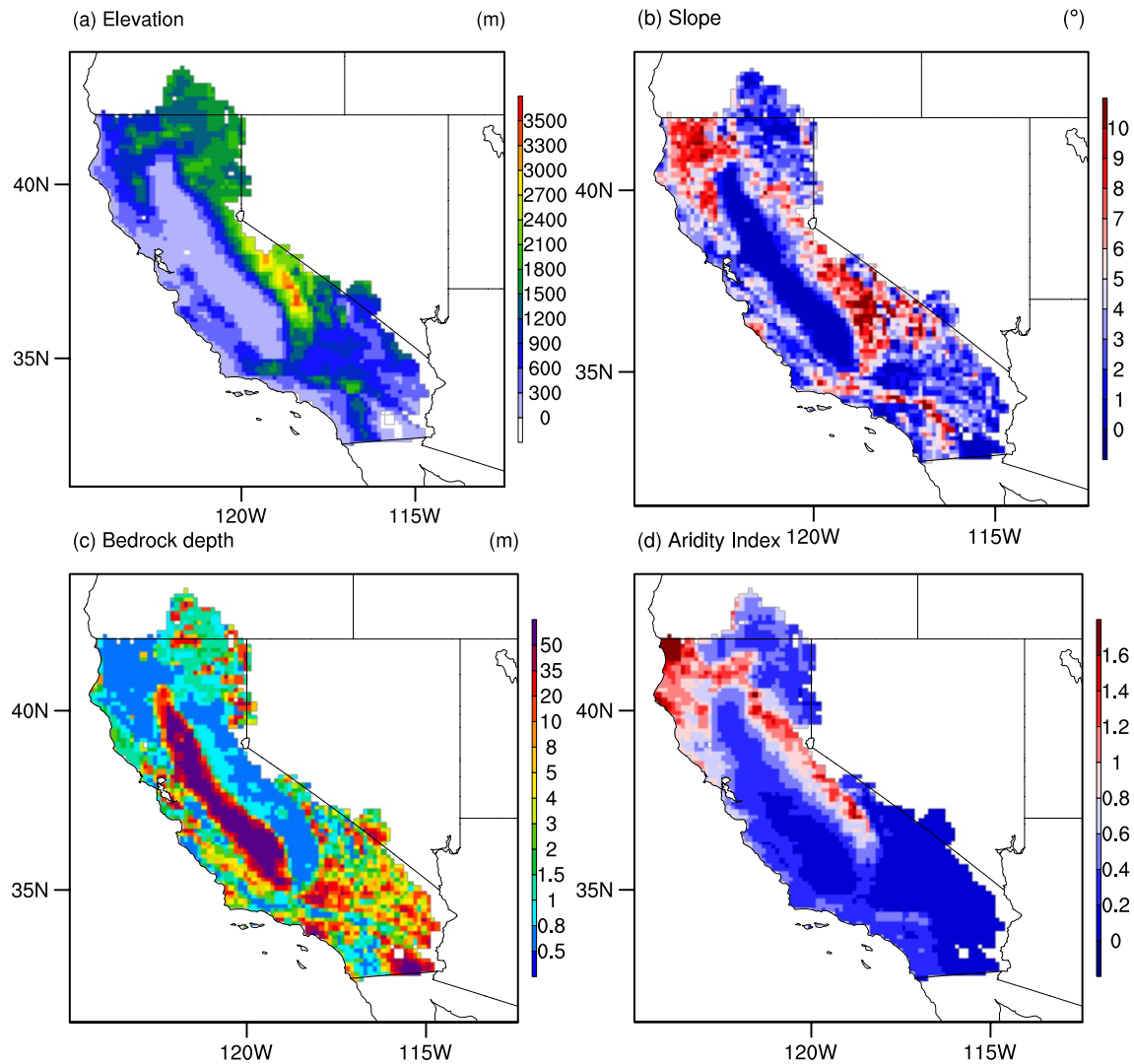
Figure 2. (a) Elevation (m), (b) topographic slope angle (in degree), (c) bedrock depth (m), and (d) aridity index (precipitation divided by potential evapotranspiration) over the HUC2-18 region.

water content and the ice impedance factor, Ω (Swenson et al., 2012), to enhance frozen soil permeability and infiltration rates; a recent study indicates that higher frozen soil permeability favors streamflow predictability due to the presence of macropores formed by ice volume expansion during freezing (Agnihotri et al., 2023).

4. We set the minimum bedrock depth as 2 m in ELM_{mod} instead of 0.2 m in $ELM_{default}$. In mountainous regions with a shallow bedrock depth (Figure 2c), infiltrated water travels through the shallow soils in a shorter period, raising the water table more rapidly than for deeper soils and thus leading to too quick surface runoff and subsurface runoff.

5. We set wetter initial conditions in ELM_{mod} to quickly achieve an equilibrium state due to higher hydraulic conductivity.

The only difference between ELM_{mod} and ELM_{H3D} is the subsurface runoff representation. We also performed multiple sensitivity experiments to investigate the impacts of alternative hillslope parameterizations (i.e., the anisotropic ratio, hillslope planforms, column numbers, and boundary conditions) on subsurface runoff generation and other water balance components. All model experiments were configured over the HUC-2 region 18 basin covering California (−124.9375°W to −112.4375°W, 31.3125°N to 43.8125°N; Figure 2) at a spatial resolution of 0.125° and a timestep of 1 hr. We ran the offline model experiments in the prescribed satellite phenology mode driven by NLDAS-2 during 1980–2015 for 8 loops (with the first 7 loops totaling 252 years as model
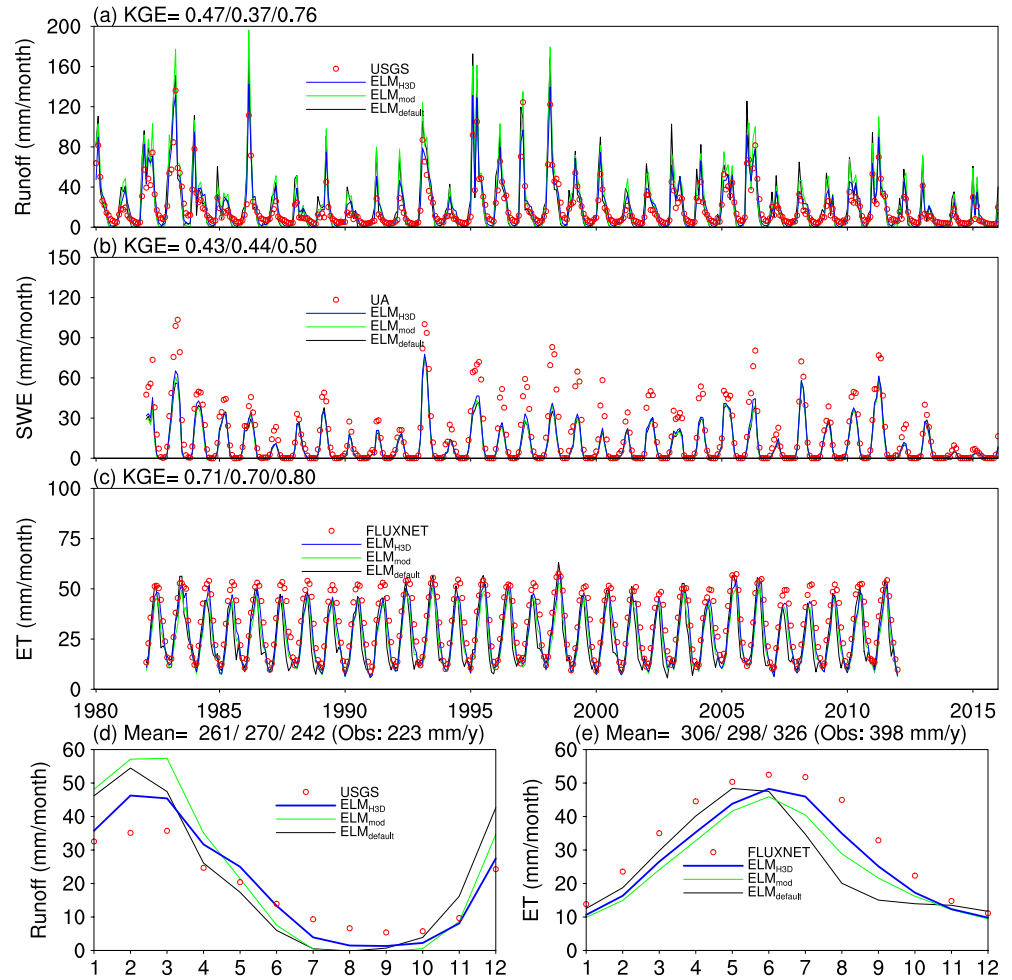
Figure 3. Monthly (a) runoff (mm/month), (b) snow water equivalent (SWE; mm/month), and (c) evapotranspiration (ET; mm/month) of observations (red circles), ELM$_{default}$ (black lines), ELM$_{mod}$ (green lines), and ELM$_{H3D}$ (blue lines) during the period of available observations. The Kling-Gupta Efficiency (KGE) values of ELM$_{default}$/ELM$_{mod}$/ELM$_{H3D}$ are provided on the top left of panel (a–c). Monthly climatology of (d) runoff and (e) ET of observations, ELM$_{default}$, ELM$_{mod}$, and ELM$_{H3D}$ with mean annual values (mm/y) on the top. Obs means observations here.

spinup) and kept monthly outputs of the last loop for the following analysis. We assessed the model performances using the Kling-Gupta Efficiency (KGE) (Gupta et al., 2009) and linear trends. The KGE metric measures the Euclidian distance of the correlations, the variabilities, and the means from the ideal points.

3. Results and Discussions

3.1. Modeled Runoff, Snow Water Equivalent, and Evapotranspiration

Figure 3 shows a comparison of modeled runoff, SWE, and ET by ELM$_{default}$, ELM$_{mod}$, and ELM$_{H3D}$ with available observations. Compared with the USGS runoff from 1980 to 2015, ELM$_{H3D}$ achieves the best KGE of 0.76, followed by ELM$_{default}$ (0.47) and ELM$_{mod}$ (0.37). The mean annual runoff of ELM$_{H3D}$, ELM$_{default}$, and ELM$_{mod}$ are 242, 261, and 270 mm, respectively, which are all greater than the observed runoff (223 mm). ELM$_{default}$ and ELM$_{mod}$ overestimate spring runoff peaks and cannot sustain later dry summer baseflow (Figures 3a and 3d) because the infiltration rates are too low. In contrast, ELM$_{H3D}$ reproduces the rising and falling runoff limbs, runoff peaks, and summer low flows. ELM$_{H3D}$ also simulates monthly ET with a higher KGE of 0.8 than ELM$_{default}$ (0.71) and ELM$_{mod}$ (0.70) during 1982–2011. ELM$_{H3D}$, ELM$_{default}$, and ELM$_{mod}$ underestimate the mean annual ET by 72 mm (18%), 92 mm (23%), and 100 mm (25%) relative to FLUXNET (398 mm), respectively. ELM$_{H3D}$
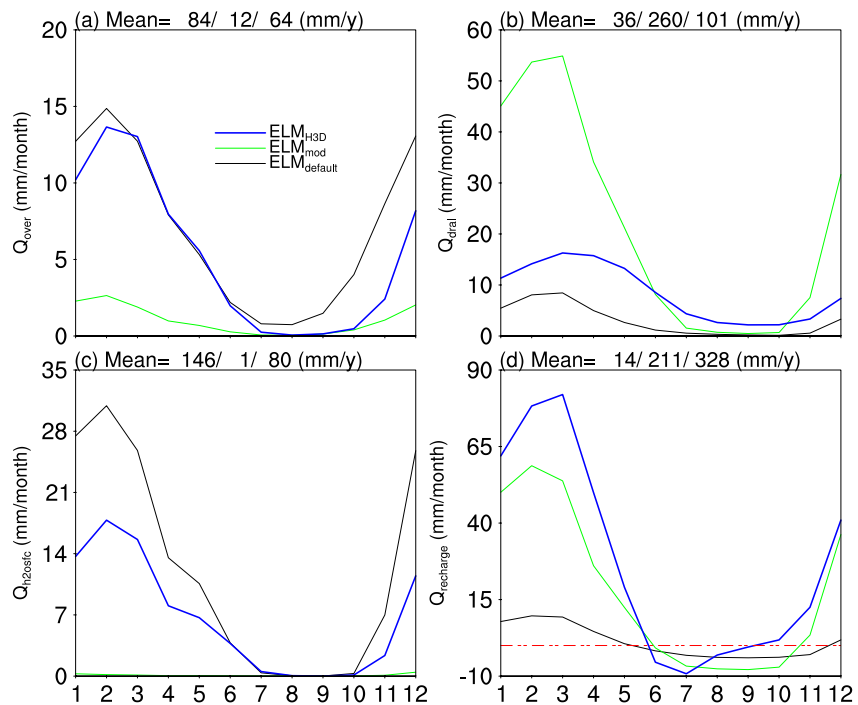
Figure 4. Monthly climatology of (a) surface saturation-excess runoff (Q_{over}; mm/month), (b) subsurface runoff (Q_{drai}; mm/month), (c) runoff of surface ponded water (Q_{h2osfc}; mm/month), and (d) groundwater recharge ($Q_{recharge}$; mm/month) of ELM$_{default}$, ELM$_{mod}$, and ELM$_{H3D}$ during 1980–2015 with mean annual values (mm/y) of ELM$_{default}$/ELM$_{mod}$/ELM$_{H3D}$ on the top of each panel. Note that the *y*-axis values differ between panels. $Q_{recharge}$ below the red dashed line indicates negative groundwater recharge (or groundwater capillary rise).

well represents the timing and magnitude of monthly ET climatology, while ELM$_{default}$ has an ET peak that is too early, and ELM$_{mod}$ generates less ET (Figure 3e). All three models show acceptable and similar SWE performance with KGEs of ~0.5 against UA SWE during 1982–2015 (Figure 3b). ELM$_{mod}$ and ELM$_{H3D}$ show slightly higher SWE because we used the Jordan (1991) snow/rain partitioning scheme instead of a linear ramp in ELM$_{default}$ (Lawrence et al., 2019) and increased the snow liquid water capacity and snow accumulation factor (Table 1). The underestimated SWE in most of the mountainous regions (Figure S1 in Supporting Information S1) is probably due to systematic precipitation and air temperature errors from NLDAS-2 (Hao et al., 2023). In summary, ELM$_{H3D}$ outperforms ELM$_{default}$ and ELM$_{mod}$ in simulating monthly runoff, SWE, and ET over the California River Basin.

Figure 4 compares the three major runoff components among the three models. ELM$_{default}$ with the original parameters values and schemes (Table 1) and the shallow bedrock depth in mountainous regions (Figure 2c) produces high saturation-excess surface runoff (Figure 4a) and runoff of surface ponded water (or infiltration-excess runoff) (Figure 4c), resulting in low groundwater recharge (Figure 4d) and subsurface runoff (or groundwater discharge, Figure 4b). With all the changes listed in Table 1, ELM$_{mod}$ produces greater infiltration, groundwater recharge (Figure 4d), and groundwater discharge as expected (Figure 4b). ELM$_{H3D}$ produces almost the same magnitude of recharge as ELM$_{mod}$ (Figure 4d) but much less groundwater discharge (Figure 4b), and the deficit is balanced by more runoff of surface ponded water (Figure 4c). The larger ponded water runoff by ELM$_{H3D}$ is due mainly to exfiltration of groundwater from lower soil columns of the hillslope, contributing to total surface runoff (Figure 4a). The negative groundwater recharge values (or groundwater capillary rise) during summer (Figure 4d) suggest that groundwater moves upward to moisten the dry soil above through capillary forces, supporting transpiration. Compared to ELM$_{mod}$, ELM$_{H3D}$ predicts a greater groundwater capillary rise during June–July, supporting the greater ET in the early drying periods (Figure 3e).
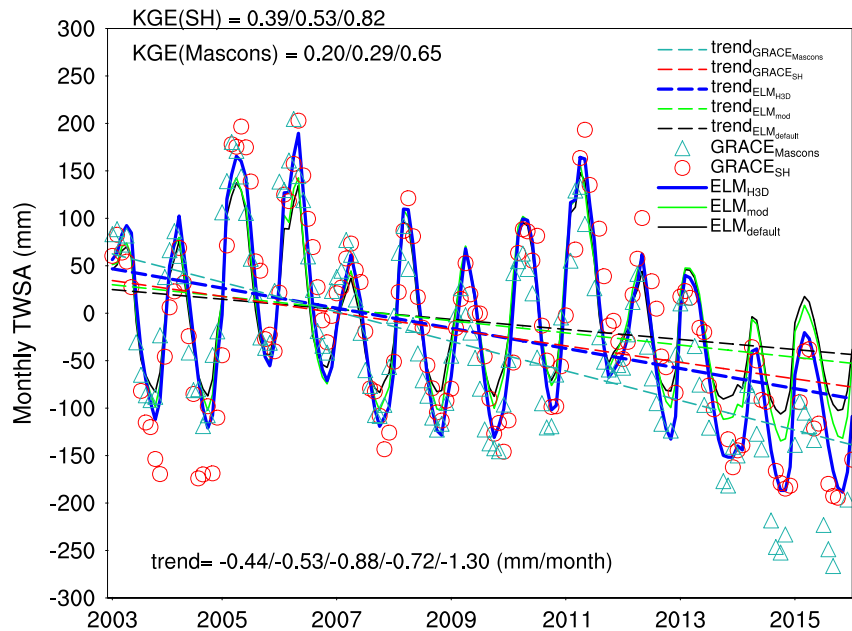
Figure 5. Monthly terrestrial water storage anomaly (TWSA; mm) of GRACE$_{SH}$ (red circles), GRACE$_{Mascons}$ (light-green triangles), ELM$_{default}$ (solid black line), ELM$_{mod}$ (solid green line), and ELM$_{H3D}$ (solid blue line) with their trend lines (dashed lines) during 2003–2015. The Kling-Gupta Efficiency (KGE) values in the order of ELM$_{default}$/ELM$_{mod}$/ELM$_{H3D}$ against GRACE$_{SH}$ are provided on the top left, below which are KGE values in the order of ELM$_{default}$/ELM$_{mod}$/ELM$_{H3D}$ against GRACE$_{Mascons}$. The linear trends of ELM$_{default}$/ELM$_{mod}$/ELM$_{H3D}$/GRACE$_{SH}$/GRACE$_{Mascons}$ are shown on the lower left (mm/month). Here, GRACE$_{SH}$ represents the averaged TWSA among JPL, CSR, and GFZ spherical harmonics (SH) solutions. GRACE$_{Mascons}$ is the averaged TWSA of JPL, CSR, and GSFC mass concentration solutions (Mascons).

3.2. Modeled Terrestrial Water Storage Anomaly

The modeled TWSA, that is, the sum of snow, canopy-intercepted water, surface ponded water, and subsurface soil water, is assessed against GRACE$_{SH}$ and GRACE$_{Mascons}$ TWSA during 2003–2015 (Figure 5). To be consistent with GRACE products, the modeled TWSA was computed by subtracting the mean monthly TWS during 2004–2009 from the monthly TWS. ELM$_{H3D}$ produces the highest KGEs (0.82 and 0.65) followed by ELM$_{mod}$ (0.53 and 0.29) and ELM$_{default}$ (0.39 and 0.20), compared to GRACE$_{SH}$ and GRACE$_{Mascons}$. ELM$_{default}$ and ELM$_{mod}$ largely underestimate seasonal and interannual TWSA variations, while ELM$_{H3D}$ matches better with both GRACE measurements, especially during the recent record-breaking drought years (2013–2015). All the three simulations, GRACE$_{SH}$, and GRACE$_{Mascons}$ show statistically significant declining trends quantified by the Mann-Kendall non-parametric test. Compared with ELM$_{default}$ (−0.44 mm/month) and ELM$_{mod}$ (−0.58 mm/month), ELM$_{H3D}$ has a drying TWSA trend (−0.88 mm/month) that is much closer to GRACE$_{SH}$ (−0.72 mm/month) and GRACE$_{Mascons}$ (−1.30 mm/month). GRACE$_{SH}$ generally suffers more signal degradation and leakage errors relative to GRACE$_{Mascons}$. Consequently, GRACE$_{SH}$ underestimates the actual decadal TWS decline and seasonal amplitudes, especially near coastal regions (Landerer & Swenson, 2012). Despite the better agreement between ELM$_{H3D}$ and the GRACE products, ELM$_{H3D}$ cannot fully capture the groundwater depletion (extremely low TWSA) probably because anthropogenic activities (e.g., groundwater pumping) are not represented in the model. Because TWSA reflects the accumulative changes of water inputs and ET loss, we compared the accumulative monthly ET during 2003–2015 among the three simulations. The accumulative ET (4,079 mm) simulated by ELM$_{H3D}$ exceeds that of ELM$_{default}$ (3,761 mm) and ELM$_{mod}$ (3,743 mm). Accumulative transpiration and soil evaporation of ELM$_{H3D}$ are 167 and 174 mm more than those of ELM$_{mod}$, respectively. Because the only difference between ELM$_{H3D}$ and ELM$_{mod}$ is the subsurface runoff treatment, this suggests that lateral subsurface flow enhances ET loss through water redistribution along hillslopes.

To better understand the enhanced ET associated with hillslope representations in ELM$_{H3D}$, we compared ET and related variables of ELM$_{H3D}$ to those of ELM$_{mod}$ spatially and temporally during the last three drought
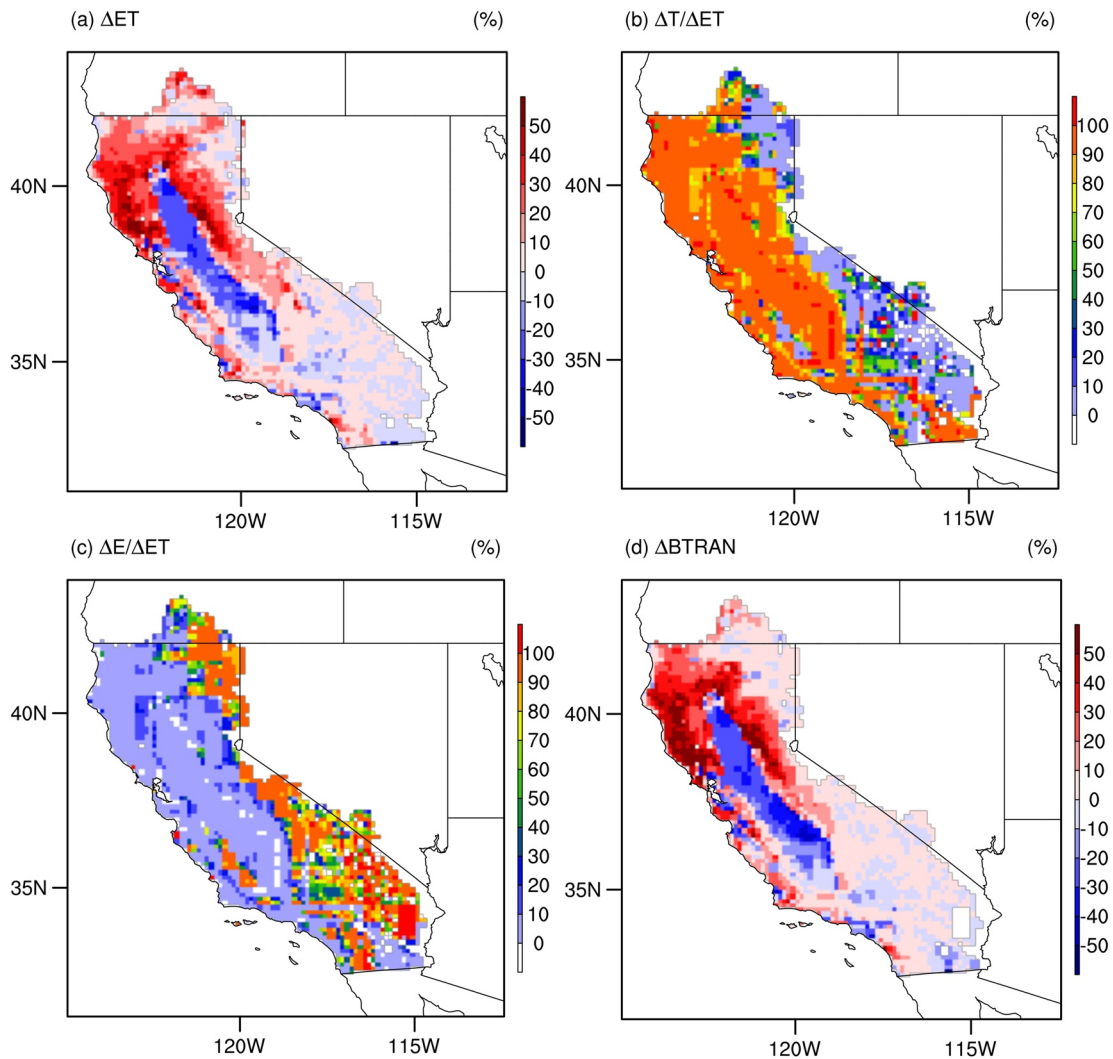
Figure 6. (a) Relative differences in summer evapotranspiration (ET) climatology (%) during 2013–2015 between ELM_{H3D} and ELM_{mod}. (b) The contribution of summer transpiration (T) climatological differences to summer ET climatological differences ($\Delta T/\Delta ET$; %) during 2013–2015. Panel (c) same as (b) but for summer soil evaporation climatological differences. Panel (d) same as (a) but for plant water stress (BTRAN), in which red indicates less water stress, and blue means the opposite.

years (2013–2015). The summer climatology difference of ET, plant transpiration, soil evaporation, and plant water stress between ELM_{H3D} and ELM_{mod} during 2013–2015 all passed the Student's t test at a confidence level of 95%. ELM_{H3D} produces up to 50% increases of ET loss compared to ELM_{mod} primarily in the mountainous regions (Figure 6a) that have relatively wet climates and moderate topographic slopes (Figure 7). Transpiration dominates the ET increases of ELM_{H3D} compared to ELM_{mod} (Figure 6b), while soil evaporation mainly contributes to the ET differences in alpine areas and desert areas (south and east of the Sierra Nevada; Figure 6c). The soil evaporation difference agrees with that of the top 10 cm soil water content (Figure 7d). ELM_{H3D} produces a higher transpiration than ELM_{mod} by reducing water stress (Figure 6d) due to more available root-zone soil water (Figure 7e).

Figure 8 describes the distribution of differences between each ELM_{H3D} column and ELM_{mod} in the summer climatology of ET and related variables during 2013–2015 for relatively steep slopes (slopes between 6° and 10°). ET and its components, plant water stress, and root-zone soil water from ELM_{H3D} show gradually smaller differences with those of ELM_{mod} from lowlands to hilltops because of flow convergence. Interestingly, all five ELM_{H3D} columns show higher transpiration relative to ELM_{mod} for 75% of the region due to less water stress associated with greater root-zone soil water. Soil evaporation simulated by ELM_{H3D} also show similar distribu-
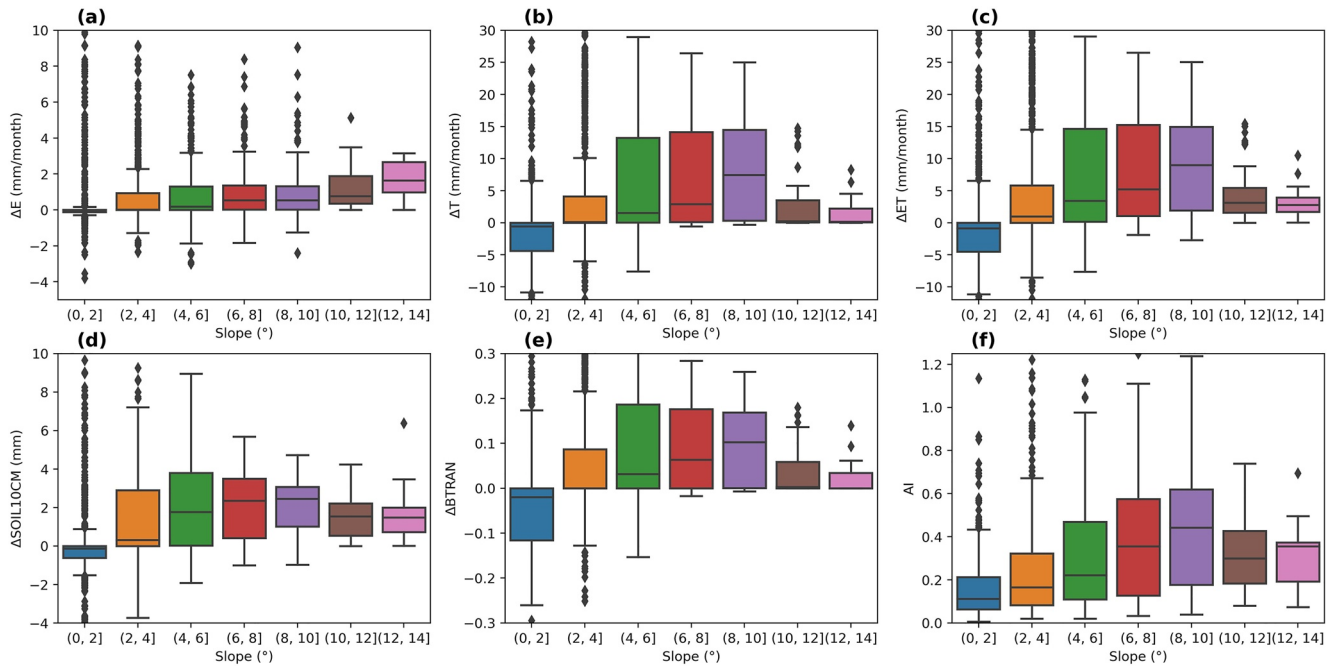
Figure 7. Summer climatology difference between ELM$_{H3D}$ and ELM$_{mod}$ during 2013–2015 in (a) soil evaporation (ΔE; mm/month), (b) transpiration (ΔT; mm/month), (c) evapotranspiration (ΔET; mm/month), (d) total soil water on the top 10 cm (ΔSOIL10CM; mm), and (e) plant water stress (ΔBTRAN) across the study region. The aridity index (AI, precipitation divided by potential evapotranspiration) is shown in (f).
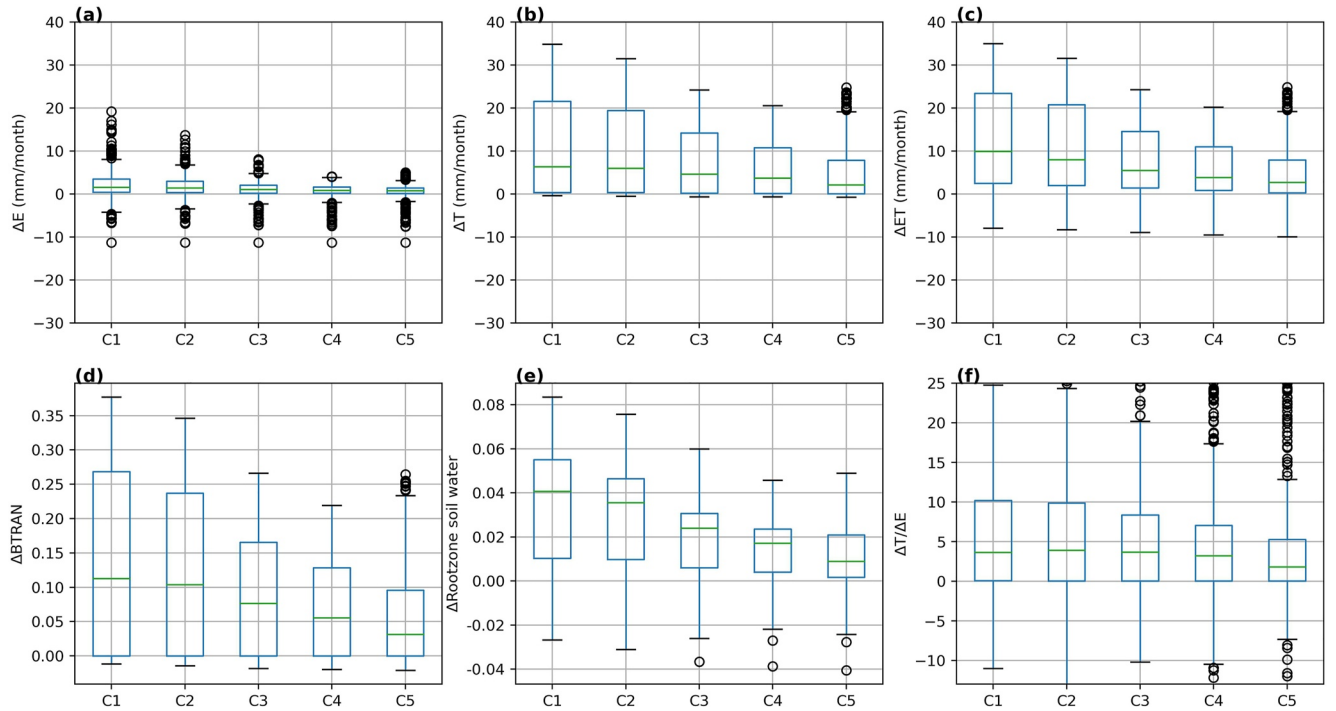

Figure 8. Summer climatology difference during 2013–2015 between each column of ELM$_{H3D}$ and ELM$_{mod}$ in (a) soil evaporation (ΔE; mm/month), (b) transpiration (ΔT; mm/month), (c) evapotranspiration (ΔET; mm/month), (c) plant water stress factor (ΔBTRAN), (e) root-zone soil water, and (d) ΔT/ΔE in regions with topographic slope between 6° and 10°. C1–C5 indicates ELM$_{H3D}$ columns from lowlands to hilltops.
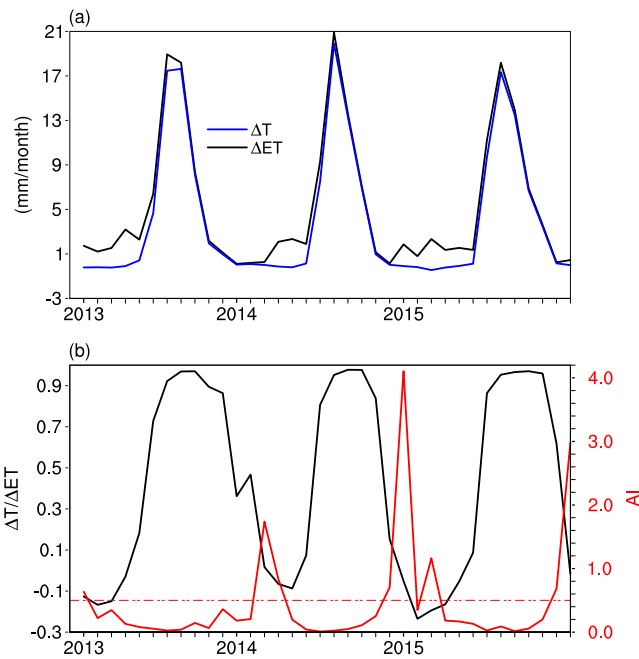
Figure 9. Monthly (a) evapotranspiration (ΔET: black line; mm/month) and transpiration difference (ΔT: blue line; mm/month) between ELM$_{H3D}$ and ELM$_{mod}$, (b) ΔT/ΔET (black line) and aridity index (AI: precipitation/potential ET; thick red line) averaged across the study region. The horizontal dashed red line represents an aridity index of 0.5, below which are dry periods.

tion patterns to transpiration. Figure 9 shows the monthly basin-averaged ET difference between ELM$_{H3D}$ and ELM$_{mod}$ and the transpiration contributions to the difference along with aridity index during 2013–2015. We defined aridity index as the ratio of precipitation to potential evapotranspiration. We found over 90% of ET increases of ELM$_{H3D}$ coming from transpiration, especially during dry summers. The dominant transpiration role reflects a strong plant drought resilience associated with water redistribution caused by lateral flow. However, the higher ET could potentially result from less runoff generated by ELM$_{H3D}$ compared to ELM$_{mod}$. To fairly evaluate the impact of hillslope on ET, we set the anisotropic ratio to 100 ($\zeta = 100$) (the Faniso100 experiment) to match the mean annual runoff (264 mm) with that of ELM$_{mod}$ (270 mm) during our simulation period (1980–2015). Surprisingly, the difference between Faniso100 and ELM$_{mod}$ in summer mean ET and its components, plant water stress, and root-zone soil water showed similar distributions like that between ELM$_{H3D}$ and ELM$_{mod}$, despite much smaller magnitudes (Figure S2 in Supporting Information S1). Summer ET and transpiration differences between Faniso100 and ELM$_{mod}$ barely change relative to the differences between ELM$_{H3D}$ and ELM$_{mod}$ in the hillslope bottom, indicating the strong resilience in the flow convergence zone. Therefore, ELM$_{H3D}$ and Faniso100 experiments demonstrate that model representations of hillslope can enhance summer ET at a spatial resolution of 1/8th degree.

3.3. Model Sensitivity Results

To explore the impacts of hillslope parameterizations on modeled water balance, we conducted four groups of additional experiments based on ELM$_{H3D}$ by changing the lateral hydraulic conductivities, idealized hillslope planforms (divergent and uniform), soil column numbers, and boundary conditions (Table 2). Lateral hydraulic conductivity is generally parameterized by multiplying the vertical saturated hydraulic conductivity with ζ on the order of 10–100 in hydrology studies (Kumar, 2004). We performed two experiments by only changing the anisotropic ratio from 10 in ELM$_{H3D}$ to 50 in Faniso50 and 100 in Faniso100. Monthly subsurface runoff peak greatly increases from ~14 mm in ELM$_{H3D}$ to ~40 and ~50 mm in Faniso50 and Faniso100, respectively (Figure 10a). Because of the fast subsurface drainage, Faniso50 and Faniso100 show less summer flows compared to ELM$_{H3D}$. Mean annual subsurface runoff of Faniso50 and Faniso100 are 94 and 126 mm more than ELM$_{H3D}$ (101 mm; Table 2), respectively. Correspondingly, surface runoff produced by Faniso50 and Faniso100 rapidly declines due to the deeper water table associated with the fast subsurface runoff (Figure S3 in Supporting Information S1).

We also found less surface water runoff in both sensitivity experiments associated with less surface water (Figure S4 in Supporting Information S1) probably due to larger infiltration capacities of drier soils (Figure S3 in Supporting Information S1). Transpiration is slightly reduced in Faniso50 and Faniso100, reflecting the strong root extractions of root-zone soil water. Also, the magnitudes of soil evaporation and transpiration in Faniso50 and Faniso100 are nearly the same as that of ELM$_{H3D}$, suggesting the impact of lateral hydraulic conductivity on ET reaching a maximum.

The Divergent and Uniform model experiments were conducted based on ELM$_{H3D}$ but with divergent and uniform planforms, respectively. Compared to ELM$_{H3D}$ with convergent planform, the Divergent and Uniform experiments show smaller subsurface runoff peaks (Figure 10b) because of the smaller hydraulic gradients associated to the divergent and uniform hillslope shapes (Figure S5 in Supporting Information S1). We found greater mean annual surface water runoff and less subsurface runoff in the Divergent and Uniform experiments (Table 2). The deeper water table (Figure S3 in Supporting Information S1) due to increased surface water runoff results in

Table 2
Annual Water Balance Components (mm/y) in the ELM$_{H3D}$ and Sensitivity Tests

Experiment	E_v	E_c	E_s	Q_{drai}	Q_{over}	Q_{h2osfc}	Q_{rgwl}	Q
ELM$_{H3D}$	226	28	69	101	64	80	−3	242
Faniso50	218	28	58	195	36	32	−3	261
Faniso100	217	28	56	227	25	16	−3	264
Uniform	228	28	73	77	42	120	−3	236
Divergent	229	27	76	61	18	157	−3	232
nh3dc10	226	28	70	97	73	74	−3	240
nh3dc20	228	28	73	85	81	74	−3	237
seepage	225	28	66	117	60	72	−3	245

Note. E_v (transpiration), E_c (canopy evaporation), E_s (soil evaporation), Q_{drai} (subsurface runoff), Q_{over} (surface runoff), Q_{h2osfc} (surface water runoff), Q_{rgwl} (surface runoff from lakes and glaciers), Q (total runoff).
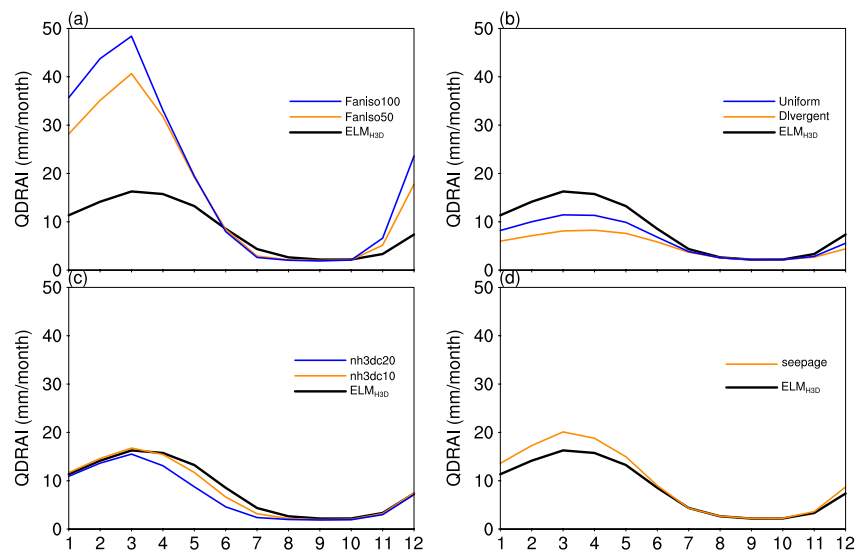
Figure 10. Monthly subsurface runoff climatology (mm/month) between ELM_{H3D} (black line) and sensitivity tests in (a) the anisotropic ratio, (b) hillslope planforms, (c) columns numbers, and (d) boundary conditions.

less surface runoff in the Divergent and Uniform experiments relative to ELM_{H3D}. Small increases of soil evaporation and transpiration probably result from longer soil water residence time through the hillslope associated with smaller hydraulic gradients (Figure S5 in Supporting Information S1).

We also changed the number of vertical soil columns for each gridcell from 5 in ELM_{H3D} to 10 (nh3dc10) and 20 (nh3dc20) to test whether the number of vertical soil columns influences modeled hillslope hydrology. Figure 10c shows slight subsurface runoff decreases in nh3dc10 and nh3dc20 during spring and summer due to smaller hydraulic gradients (Figure S5 in Supporting Information S1). The mean annual subsurface runoff is 97 and 85 mm, respectively. Mean annual surface runoff is slightly increased in both experiments due to shallower water tables compared with ELM_{H3D} (Figure S3 in Supporting Information S1). However, ET components and surface water runoff are barely changed. In summary, it is not necessary to have more than five soil columns to reflect the hillslope water balance well on the current model horizontal grid size of 1/8°.

The lower boundary conditions at the seepage face of the hillslope directly influences the water exchanges between the hillslope bottom and river channel. Currently, ELM_{H3D} assumes zero total hydraulic gradients between the lowest soil column and river channels. Since we have not coupled ELM_{H3D} with the ELM river transport model (Li et al., 2013), we performed an experiment with extreme conditions of zero flow in the river channel (seepage). In other words, groundwater freely travels through the interface between the hillslope lower boundary and river channels. The seepage experiment shows higher subsurface runoff mainly in wet seasons compared with ELM_{H3D} (Figure 10d). Mean annual subsurface runoff is increased from 101 mm (ELM_{H3D}) to 117 mm in the seepage experiment. Mean annual surface runoff, soil evaporation, and transpiration are hardly changed from those of ELM_{H3D}. Mean annual surface water runoff is reduced because of the enhanced infiltration capacity reflected by deeper water tables (Figure S3 in Supporting Information S1).

4. Discussion

Our sensitivity tests suggest that subsurface runoff is most sensitive to the anisotropic factor, ζ (or lateral saturated hydraulic conductivities, $k_{s,l}$). Numerous laboratory-based and field-based methods have been developed to measure small-scale (e.g., small soil cores) $k_{s,l}$ (Dorsey et al., 1990; Mohanty et al., 1994; Youngs, 1987). However, small-scale $k_{s,l}$ measurements consistently underestimate large-scale (e.g., hillslope-scale) $k_{s,l}$ due to the lack of information about spatial heterogeneity, especially in the fields where macropores are present (Brooks et al., 2004). Due to the high experimental cost, only a few studies have estimated hillslope-scale $k_{s,l}$ through trench and drains experiments (Brooks et al., 2004; Chappell & Lancaster, 2007; Dunne & Black, 1970;

Pirastru et al., 2022). Therefore, modelers usually calibrate $k_{s,l}$ based on streamflow/baseflow or simply by relating ζ with the clay content (Beven et al., 1995; Chen & Kumar, 2001; Fan et al., 2007; Grayson et al., 1992; Kumar, 2004; Wigmosta et al., 1994; Zeng et al., 2016). In this study, we manually calibrated ζ to a value of 10 (spatially constant) by matching the simulated runoff with the observed monthly runoff. We also conducted an additional ELM_{H3D} run that parameterizes ζ as the clay percentage from the ELM surface input. However, this run performed worse than the one with our manually calibrated ζ (=10) (figures not shown). Undoubtedly, these calibrated $k_{s,l}$ may not represent the actual large-scale $k_{s,l}$ due to the intrinsic uncertainties in model structure and parameter (Beven et al., 1995; Grayson et al., 1992). To realistically parameterize $k_{s,l}$, modelers and field hydrologists should work together to experimentally determine $k_{s,l}$ at the scale of modeling domain if applicable (Brooks et al., 2004; Pirastru et al., 2022). Besides large-scale $k_{s,l}$ measurements, pedotransfer functions connecting $k_{s,l}$ with easily-observed variables (e.g., soil properties, vegetation, and climates) and upscaling methods might be necessary for global applications (Chen & Kumar, 2001).

In this study, we assigned each grid cell with a single representative hillslope that was simplified through a width distribution function without accounting for land surface heterogeneities along the hillslope. Many methods have been developed to realistically group hydrologically similar areas that are primarily controlled by topography, such as elevation bands (Ke et al., 2013; Nijssen et al., 1997), topographic units (Tesfa & Leung, 2017), height above nearest drainage area bands (Nobre et al., 2011), and by using clustering approaches (Chaney et al., 2016; Newman et al., 2014). Recently, gridcell-based and catchment-based hierarchical multivariate clustering methods have been developed to generate hydrologically connected characteristic hillslopes with explicit hillslope-scale surface heterogeneities defined (Chaney et al., 2018, 2021; Huang et al., 2022). These advanced spatial tessellation methods combined with various climate downscaling methods (Gaur & Simonovic, 2018; Tesfa et al., 2020) can better derive representative hillslopes to represent hillslope-scale hydrology in ELM_{H3D} for the future work.

While we made multiple assumptions in parametrizing representative hillslopes and lateral flow movement, ELM_{H3D} represents a step toward more realistic and mechanistic description of hillslope-scale hydrology in large-scale global models (e.g., E3SM). Instead of a straightforward application of Darcy's law to describe lateral flow along representative hillslopes in ESMs like many other studies (Chaney et al., 2016, 2018, 2021; Subin et al., 2014; Swenson et al., 2019), the hsB model combines the Darcy's law with the continuity equation and explicitly accounts for hillslope shapes that can approximate 2-D hillslope lateral flow through a 1-D equation (Troch et al., 2003). The hsB lateral flow scheme coupled with the 1-D Richards equation (i.e., H3D) has demonstrated comparable accuracy with the 3-D CATHY model but reduces computation time by up to 2–3 orders of magnitude (Hazenberg et al., 2015, 2016; Troch et al., 2003). Compared to $ELM_{default}$, the additional computation cost in ELM_{H3D} is primarily caused by increasing the number of vertical soil columns to describe the representative hillslopes. Currently, ELM_{H3D} with 5 vertical soil columns only takes twice as much time to run at the same configuration as $ELM_{default}$. The adaptive time stepping scheme used in ELM_{H3D} ensures the computational efficiency and stability for both regional and global simulations.

To understand the impact of lateral flow on the ecosystem, we analyzed the modeled soil moisture and water table depth. The modeled surface soil moisture (0–10 cm) of ELM_{H3D} and ELM_{mod} agree with that of an observation-based product (Wang et al., 2021) over California during 1980–2015 (Figure S6 in Supporting Information S1). Only slight difference in surface soil moisture between ELM_{H3D} and ELM_{mod} exists because lateral flow mainly affects the saturated zone, instead of the soil surface. ELM_{H3D} produces deeper water table over the Central Valley relative to ELM_{mod} due to the different schemes of groundwater discharge used in the two models. Groundwater discharge in ELM_{H3D}, which is simulated by hsB with the seepage (or equilibrium) lateral boundary condition at the hillslope bottom, is independent of the water table depth, and therefore, the model produces greater groundwater discharge despite small topographical relief in the valley. However, ELM_{mod} with the TOPMODEL baseflow scheme, which is an exponential function of the water table depth, produces negligible discharge when the water table depth is deep (for instance >10 m). In addition, the deeper water table in the valley modeled by ELM_{H3D} can be attributed to the deficiencies in representing lateral water transport between model grids. All model simulations generate much shallower water table up in the mountains than that of Fan et al. (2013) because of the depth-to-bedrock data set (Pelletier et al., 2016) used as the lower boundary of the model (Figure S7 in Supporting Information S1; Figure 2c). Further studies need to combine more observations of the critical zone (e.g., soil depth and hydraulic properties) with model representations of groundwater
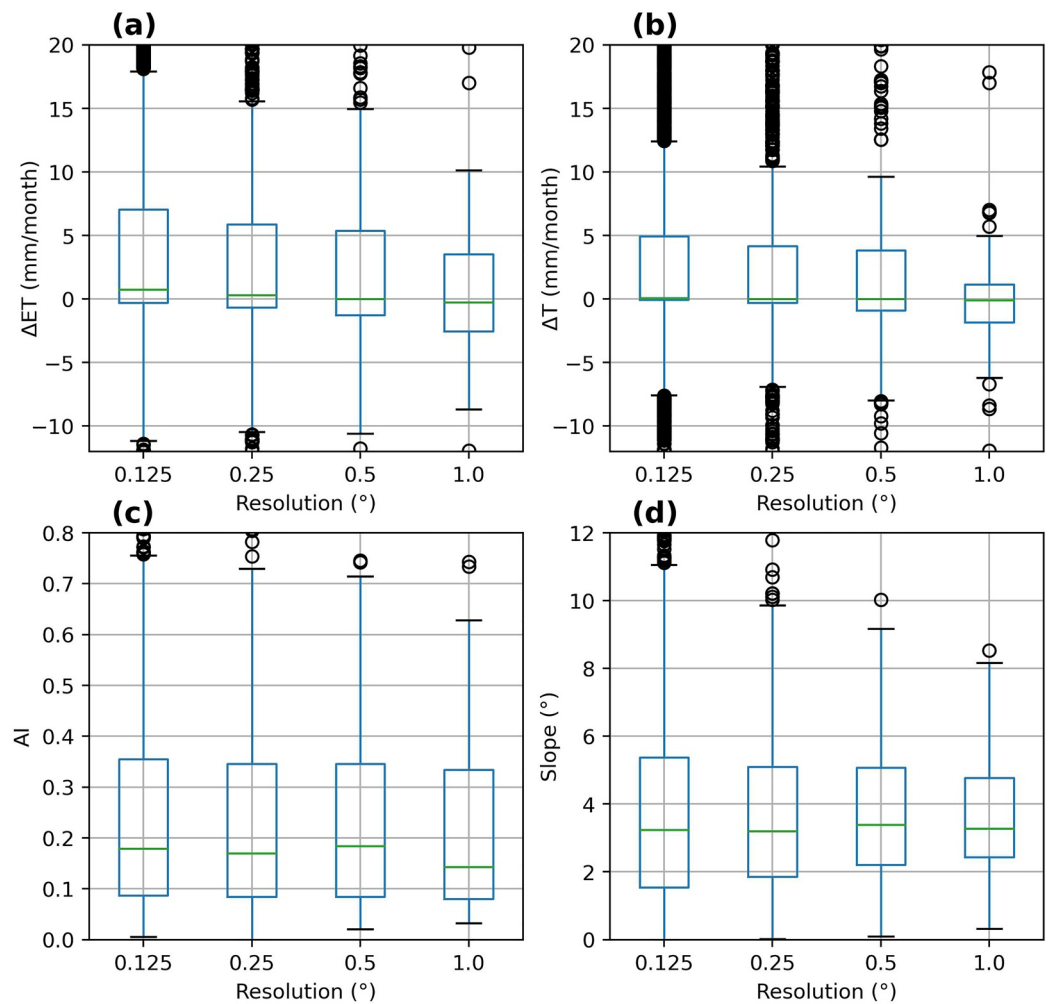
Figure 11. Summer climatology difference in (a) evapotranspiration (ΔET; mm/month) and (b) transpiration (ΔT; mm/month) during 2013–2015 between ELM$_{H3D}$ and ELM$_{mod}$ at grid sizes of 0.125, 0.25, 0.5, and 1°; (c) aridity index (precipitation divided by potential ET) and (d) slope (°) distributions at grid sizes of 0.125, 0.25, 0.5, and 1° over the California basin.

lateral flow between grids and interactions with river water level to improve the modeled water table depth (Fan et al., 2019).

Previous studies have shown the importance of lateral flow on transpiration partitioning and ecosystem productivities through computationally more expensive model experiments at hyper resolutions with explicit 3-D groundwater models (Chang et al., 2018; Maxwell & Condon, 2016). ELM$_{H3D}$ is not only computationally efficient at coarser resolutions but also able to represent the effects of groundwater lateral flow movement on ecosystem drought response, paving the way to representations of the ecohydrological effects in global models. The better modeled TWSA decline by ELM$_{H3D}$ highlights the necessity of lateral groundwater flow model representation because most ESMs and large-scale hydrological models substantially underestimate the observed drying TWSA trends globally (Scanlon et al., 2018). Consistent with Fan et al. (2019), greater transpiration enhancement in ELM$_{H3D}$ occurred in regions characterized with seasonally dry climates (dry summers following wet winters and springs) and moderate topographic slopes (Figures 6–8). We also conducted ELM$_{H3D}$ experiments at 0.25-degree, 0.5-degree, and 1-degree resolution to explore the impacts of horizontal grid size on modeled ET during drought years. Modeled ET enhancements caused by lateral groundwater flow decrease with increasing grid size and almost disappear with a grid size of 1°, potentially resulting from unrepresentative climates and unresolved land surface properties (Figure 11). This suggests that more effective and accurate subgrid representations of land

surface characteristics and climatic forcing are required to fully reflect the ecosystem responses to lateral groundwater flow for coarser resolution models.

5. Conclusion

In summary, we implemented the lateral saturated flow model of a hybrid-3D hydrological hillslope model into ELMv1 to explicitly represent hillslope-scale hydrological rainfall-runoff responses with acceptable computational costs. Despite the simplifications (compared with a full 3-D hydrological model), the new model exhibits better hydrological performances in simulating runoff, ET, and TWSA over the California Basin than models without representations of lateral flow along hillslopes. The redistribution of soil water along hillslopes driven by topographic relief results in higher transpiration and ET over the mountainous regions with mediate topographic slopes and seasonally dry climates than at the hilltops, which cannot be achieved without an explicit lateral flow representation. As a result, our new model can better reproduce the declining trend of the GRACE TWSA by enhancing ecosystem drought resilience caused by water convergence through terrain-driven lateral groundwater flow. Our model produces much greater ET than ELM_{mod}, particularly during the dry period from 2013 to 2015 with more than 90% of the ET increase coming from plant transpiration. The magnitude of enhanced ET from ELM_{H3D} is positively correlated with topographic slope angles. This study indicates that models which do not explicitly represent subgrid lateral groundwater flow may underestimate transpiration-dominated ET during droughts over mountainous regions.

Appendix A

The numerical equation of the hsB on the seepage face of the lower lateral boundary (Figure A1):

$$f \frac{\partial h}{\partial t} = \frac{1}{w_0} \frac{1}{\Delta x_0} [(\sin\, \alpha)(w_{0.5}k_{0.5}h_{0.5} - w_{-0.5}k_{-0.5}h_{-0.5})$$
$$+ (\cos\, \alpha)\left(w_{0.5}k_{0.5}h_{0.5} \frac{h_1 - h_0}{x_1 - x_0} - (Q_{seepage} + Q_{saturated}) \right)]$$

where f is the drainable porosity. h (m) is the height of the saturated zone perpendicular to the hillslope bedrock with a slope angle α. w (m) is the width of the hillslope at a given distance x (m) from the outflow point. k (m/s) is the lateral saturated hydraulic conductivity at height h. The subscripts of 0, 0.5, and -0.5 represent the center, upper boundary, and lower boundary of the lowest column. Here, seepage flux means the water flux traveling
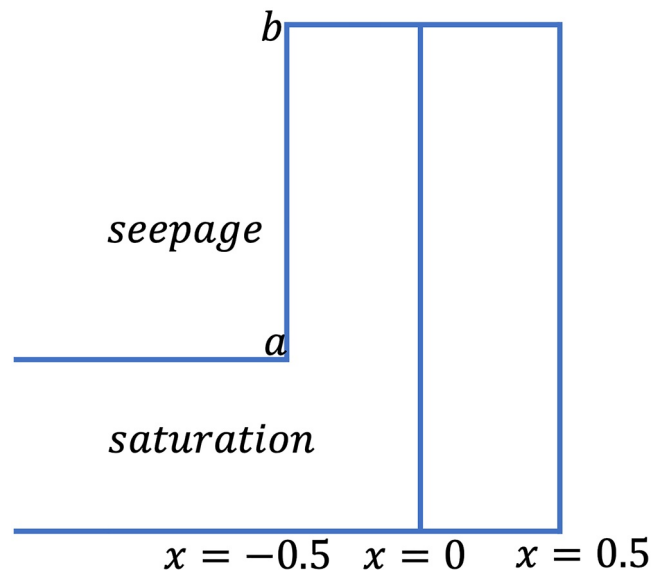

Figure A1. The seepage face of the lowest column directly connecting rivers. b and a represent the water table height of the lowest column and the river height at the lower boundary of the lowest column ($x = -0.5$), respectively. $x = 0$ indicates the column center, and $x = 0.5$ means the upper boundary of the lowest column.

in the interface between soil unsaturated zone and air. The saturated flux means the water flux traveling in the interface between soil saturated zone and river. We assumed the river is dry in the seepage experiment, that is, saturated flux is zero.

$$Q_{seepage} = w_{-0.5} \int_a^b k_{-0.5} \frac{(h_0 - (h_{-1} + z - a))}{0.5 \Delta x_0} dz = w_{-0.5} k_{-0.5} \frac{h_0^2}{\Delta x_0}$$

where a is the bottom of the saturated zone ($a = 0$) of the lower boundary (m). b is the top of the saturated zone of the lower boundary (m), and h_0 is the total head on the center of the saturated zone in the lowest column (m). $b = h_0$. Δx_0 is the length of the lowest column (m). $w_{-0.5}$ is the lowest column width on the lower lateral boundary.

Data Availability Statement

The data used in this study are all available online: NLDAS-2 data (http://www.emc.ncep.noaa.gov/mmb/nldas/); the FLUXNET-MTE ET data (https://www.bgc-jena.mpg.de/bgi/index.php/Services/Overview); the University of Arizona SWE data (https://nsidc.org/data/nsidc-0719/versions/1); the monthly USGS Water Watch hydrological unit runoff data (https://waterwatch.usgs.gov/); the GRACE TWSA data (http://grace.jpl.nasa.gov); the JPL GRACE/GRACE-FO RL06 Mascon Solutions (https://grace.jpl.nasa.gov/data/get-data/jpl_global_mascons/); the CSR GRACE/GRACE-FO RL06 Mascon Solutions (http://www2.csr.utexas.edu/grace); the GSFC GRACE/GRACE-FO RL06 Mascon Solutions (https://earth.gsfc.nasa.gov/geo/data/grace-mascons). The ELMv1 code can be downloaded from http://github.com/E3SM-Project/E3SM.

References

Agnihotri, J., Behrangi, A., Tavakoly, A., Geheran, M., Farmani, M. A., & Niu, G. Y. (2023). Higher frozen soil permeability represented in a hydrological model improves spring streamflow prediction from River Basin to continental scales. *Water Resources Research*, *59*(4), e2022WR033075. https://doi.org/10.1029/2022wr033075

Arboleda Obando, P. F., Ducharne, A., Cheruy, F., Jost, A., Ghattas, J., Colin, J., & Nous, C. (2022). Influence of hillslope flow on hydroclimatic evolution under climate change. *Earth's Future*, *10*(9), e2021EF002613. https://doi.org/10.1029/2021ef002613

Ault, T. R., Mankin, J. S., Cook, B. I., & Smerdon, J. E. (2016). Relative impacts of mitigation, temperature, and precipitation on 21st-century megadrought risk in the American Southwest. *Science Advances*, *2*(10), e1600873. https://doi.org/10.1126/sciadv.1600873

Barlage, M., Chen, F., Rasmussen, R., Zhang, Z., & Miguez-Macho, G. (2021). The importance of scale-dependent groundwater processes in land-atmosphere interactions over the central United States. *Geophysical Research Letters*, *48*(5), e2020GL092171. https://doi.org/10.1029/2020gl092171

Beven, K., Lamb, R., Quinn, P., Romanowicz, R., & Freer, J. (1995). Topmodel. In *Computer models of watershed hydrology* (pp. 627–668).

Beven, K. J., & Kirkby, M. J. (1979). A physically based, variable contributing area model of basin hydrology/Un modèle à base physique de zone d'appel variable de l'hydrologie du bassin versant. *Hydrological Sciences Journal*, *24*(1), 43–69. https://doi.org/10.1080/02626667909491834

Bisht, G., Huang, M., Zhou, T., Chen, X., Dai, H., Hammond, G. E., et al. (2017). Coupling a three-dimensional subsurface flow and transport model with a land surface model to simulate stream–aquifer–land interactions (CP v1. 0). *Geoscientific Model Development*, *10*(12), 4539–4562. https://doi.org/10.5194/gmd-10-4539-2017

Brakebill, J., Wolock, D., & Terziotti, S. (2011). Digital hydrologic networks supporting applications related to spatially referenced regression modeling 1. *JAWRA Journal of the American Water Resources Association*, *47*(5), 916–932. https://doi.org/10.1111/j.1752-1688.2011.00578.x

Brooks, E. S., Boll, J., & McDaniel, P. A. (2004). A hillslope-scale experiment to measure lateral saturated hydraulic conductivity. *Water Resources Research*, *40*(4), W04208. https://doi.org/10.1029/2003wr002858

Broxton, P. D., Dawson, N., & Zeng, X. (2016). Linking snowfall and snow accumulation to generate spatial maps of SWE and snow depth. *Earth and Space Science*, *3*(6), 246–256. https://doi.org/10.1002/2016ea000174

Chaney, N. W., Metcalfe, P., & Wood, E. F. (2016). HydroBlocks: A field-scale resolving land surface model for application over continental extents. *Hydrological Processes*, *30*(20), 3543–3559. https://doi.org/10.1002/hyp.10891

Chaney, N. W., Torres-Rojas, L., Vergopolan, N., & Fisher, C. K. (2021). HydroBlocks v0. 2: Enabling a field-scale two-way coupling between the land surface and river networks in Earth system models. *Geoscientific Model Development*, *14*(11), 6813–6832. https://doi.org/10.5194/gmd-14-6813-2021

Chaney, N. W., Van Huijgevoort, M. H., Shevliakova, E., Malyshev, S., Milly, P. C., Gauthier, P. P., & Sulman, B. N. (2018). Harnessing big data to rethink land heterogeneity in Earth system models. *Hydrology and Earth System Sciences*, *22*(6), 3311–3330. https://doi.org/10.5194/hess-22-3311-2018

Chang, L. L., Dwivedi, R., Knowles, J. F., Fang, Y. H., Niu, G. Y., Pelletier, J. D., et al. (2018). Why do large-scale land surface models produce a low ratio of transpiration to evapotranspiration? *Journal of Geophysical Research: Atmospheres*, *123*(17), 9109–9130. https://doi.org/10.1029/2018jd029159

Chappell, N. A., & Lancaster, J. W. (2007). Comparison of methodological uncertainties within permeability measurements. *Hydrological Processes: International Journal*, *21*(18), 2504–2514. https://doi.org/10.1002/hyp.6416

Chen, J., & Kumar, P. (2001). Topographic influence on the seasonal and interannual variation of water and energy balance of basins in North America. *Journal of Climate*, *14*(9), 1989–2014. https://doi.org/10.1175/1520-0442(2001)014<1989:tiotsa>2.0.co;2

Cook, B. I., Williams, A. P., Smerdon, J. E., Palmer, J. G., Cook, E. R., Stahle, D. W., & Coats, S. (2018). Cold tropical Pacific sea surface temperatures during the late sixteenth-century North American megadrought. *Journal of Geophysical Research: Atmospheres*, *123*(20), 11307–11320. https://doi.org/10.1029/2018jd029323

Dawson, N., Broxton, P., & Zeng, X. (2017). A new snow density parameterization for land data initialization. *Journal of Hydrometeorology*, *18*(1), 197–207. https://doi.org/10.1175/jhm-d-16-0166.1

Dong, J., Lei, F., & Crow, W. T. (2022). Land transpiration-evaporation partitioning errors responsible for modeled summertime warm bias in the central United States. *Nature Communications*, *13*(1), 336. https://doi.org/10.1038/s41467-021-27938-6

Dorsey, J., Ward, A., Fausey, N., & Bair, E. (1990). A comparison of four field methods for measuring saturated hydraulic conductivity. *Transactions of the ASAE*, *33*(6), 1925–1931. https://doi.org/10.13031/2013.31560

Dunne, T., & Black, R. D. (1970). An experimental investigation of runoff production in permeable soils. *Water Resources Research*, *6*(2), 478–490. https://doi.org/10.1029/wr006i002p00478

Famiglietti, J., & Wood, E. F. (1991). Evapotranspiration and runoff from large land areas: Land surface hydrology for atmospheric general circulation models. *Surveys in Geophysics*, *12*(1–3), 179–204. https://doi.org/10.1007/bf01903418

Famiglietti, J., & Wood, E. F. (1994). Multiscale modeling of spatially variable water and energy balance processes. *Water Resources Research*, *30*(11), 3061–3078. https://doi.org/10.1029/94wr01498

Fan, Y., & Bras, R. L. (1998). Analytical solutions to hillslope subsurface storm flow and saturation overland flow. *Water Resources Research*, *34*(4), 921–927. https://doi.org/10.1029/97wr03516

Fan, Y., Clark, M., Lawrence, D. M., Swenson, S., Band, L., Brantley, S. L., et al. (2019). Hillslope hydrology in global change research and earth system modeling. *Water Resources Research*, *55*(2), 1737–1772. https://doi.org/10.1029/2018wr023903

Fan, Y., Li, H., & Miguez-Macho, G. (2013). Global patterns of groundwater table depth. *Science*, *339*(6122), 940–943. https://doi.org/10.1126/science.1229881

Fan, Y., Miguez-Macho, G., Weaver, C. P., Walko, R., & Robock, A. (2007). Incorporating water table dynamics in climate modeling: 1. Water table observations and equilibrium water table simulations. *Journal of Geophysical Research*, *112*(D10), D10125. https://doi.org/10.1029/2006jd008111

Felfelani, F., Lawrence, D. M., & Pokhrel, Y. (2021). Representing intercell lateral groundwater flow and aquifer pumping in the community land model. *Water Resources Research*, *57*(1), e2020WR027531. https://doi.org/10.1029/2020wr027531

Feng, S., Hu, Q., & Oglesby, R. J. (2011). Influence of Atlantic sea surface temperatures on persistent drought in North America. *Climate Dynamics*, *37*(3–4), 569–586. https://doi.org/10.1007/s00382-010-0835-x

Gaur, A., & Simonovic, S. P. (2018). Application of physical scaling towards downscaling climate model precipitation data. *Theoretical and Applied Climatology*, *132*(1–2), 287–300. https://doi.org/10.1007/s00704-017-2088-7

Govind, A., Chen, J. M., McDonnell, J., Kumari, J., & Sonnentag, O. (2011). Effects of lateral hydrological processes on photosynthesis and evapotranspiration in a boreal ecosystem. *Ecohydrology*, *4*(3), 394–410. https://doi.org/10.1002/eco.141

Grayson, R. B., Moore, I. D., & Mcmahon, T. A. (1992). Physically based hydrologic modeling: 1. A terrain-based model for investigative purposes. *Water Resources Research*, *28*(10), 2639–2658. https://doi.org/10.1029/92wr01258

Gupta, H. V., Kling, H., Yilmaz, K. K., & Martinez, G. F. (2009). Decomposition of the mean squared error and NSE performance criteria: Implications for improving hydrological modelling. *Journal of Hydrology*, *377*(1–2), 80–91. https://doi.org/10.1016/j.jhydrol.2009.08.003

Hao, D., Bisht, G., Rittger, K., Stillinger, T., Bair, E., Gu, Y., & Leung, L. R. (2023). Evaluation of E3SM land model snow simulations over the western United States. *The Cryosphere*, *17*(2), 673–697. https://doi.org/10.5194/tc-17-673-2023

Hazenberg, P., Broxton, P., Gochis, D., Niu, G. Y., Pangle, L., Pelletier, J., et al. (2016). Testing the hybrid-3-D hillslope hydrological model in a controlled environment. *Water Resources Research*, *52*(2), 1089–1107. https://doi.org/10.1002/2015wr018106

Hazenberg, P., Fang, Y., Broxton, P., Gochis, D., Niu, G. Y., Pelletier, J., et al. (2015). A hybrid-3D hillslope hydrological model for use in Earth system models. *Water Resources Research*, *51*(10), 8218–8239. https://doi.org/10.1002/2014wr016842

Hilberts, A. G., van Loon, E. E., Troch, P. A., & Paniconi, C. (2004). The hillslope-storage Boussinesq model for non-constant bedrock slope. *Journal of Hydrology*, *291*(3–4), 160–173. https://doi.org/10.1016/j.jhydrol.2003.12.043

Hong, S.-Y., & Kalnay, E. (2000). Role of sea surface temperature and soil-moisture feedback in the 1998 Oklahoma–Texas drought. *Nature*, *408*(6814), 842–844. https://doi.org/10.1038/35048548

Hoylman, Z. H., Jencso, K. G., Hu, J., Martin, J. T., Holden, Z. A., Seielstad, C. A., & Rowell, E. M. (2018). Hillslope topography mediates spatial patterns of ecosystem sensitivity to climate. *Journal of Geophysical Research: Biogeosciences*, *123*(2), 353–371. https://doi.org/10.1002/2017jg004108

Huang, L., Zhang, S., Niu, G. Y., Wei, N., Yuan, H., Wei, Z., et al. (2022). A catchment-based hierarchical spatial tessellation approach to a better representation of land heterogeneity for hyper-resolution land surface modeling. *Water Resources Research*, *58*(5), e2021WR031589. https://doi.org/10.1029/2021wr031589

Ji, P., Yuan, X., & Liang, X. Z. (2017). Do lateral flows matter for the hyperresolution land surface modeling? *Journal of Geophysical Research: Atmospheres*, *122*(22), 12077–12092. https://doi.org/10.1002/2017jd027366

Jordan, R. E. (1991). A one-dimensional temperature model for a snow cover: Technical documentation for SNTHERM (Vol. *89*).

Joyce, R. J., Janowiak, J. E., Arkin, P. A., & Xie, P. (2004). CMORPH: A method that produces global precipitation estimates from passive microwave and infrared data at high spatial and temporal resolution. *Journal of Hydrometeorology*, *5*(3), 487–503. https://doi.org/10.1175/1525-7541(2004)005<0487:camtpg>2.0.co;2

Jung, M., Reichstein, M., Margolis, H. A., Cescatti, A., Richardson, A. D., Arain, M. A., et al. (2011). Global patterns of land-atmosphere fluxes of carbon dioxide, latent heat, and sensible heat derived from eddy covariance, satellite, and meteorological observations. *Journal of Geophysical Research*, *116*(G3), G00J07. https://doi.org/10.1029/2010jg001566

Ke, Y., Leung, L., Huang, M., & Li, H. (2013). Enhancing the representation of subgrid land surface characteristics in land surface models. *Geoscientific Model Development Discussions*, *6*(1), 2177–2212. https://doi.org/10.5194/gmd-6-1609-2013

Kollet, S. J., & Maxwell, R. M. (2008). Capturing the influence of groundwater dynamics on land surface processes using an integrated, distributed watershed model. *Water Resources Research*, *44*(2), W02402. https://doi.org/10.1029/2007wr006004

Koster, R. D., Suarez, M. J., Ducharne, A., Stieglitz, M., & Kumar, P. (2000). A catchment-based approach to modeling land surface processes in a general circulation model: 1. Model structure. *Journal of Geophysical Research*, *105*(D20), 24809–24822. https://doi.org/10.1029/2000jd900327

Koster, R. D., Suarez, M. J., & Heiser, M. (2000). Variance and predictability of precipitation at seasonal-to-interannual timescales. *Journal of Hydrometeorology*, *1*(1), 26–46. https://doi.org/10.1175/1525-7541(2000)001<0026:vapopa>2.0.co;2

Krakauer, N. Y., Li, H., & Fan, Y. (2014). Groundwater flow across spatial scales: Importance for climate modeling. *Environmental Research Letters*, *9*(3), 034003. https://doi.org/10.1088/1748-9326/9/3/034003

Kuffour, B. N., Engdahl, N. B., Woodward, C. S., Condon, L. E., Kollet, S., & Maxwell, R. M. (2020). Simulating coupled surface–subsurface flows with ParFlow v3. 5.0: Capabilities, applications, and ongoing development of an open-source, massively parallel, integrated hydrologic model. *Geoscientific Model Development*, *13*(3), 1373–1397. https://doi.org/10.5194/gmd-13-1373-2020

Kumar, P. (2004). Layer averaged Richard's equation with lateral flow. *Advances in Water Resources*, *27*(5), 521–531. https://doi.org/10.1016/j.advwatres.2004.02.007

Landerer, F. W., & Swenson, S. (2012). Accuracy of scaled GRACE terrestrial water storage estimates. *Water Resources Research*, *48*(4), W04531. https://doi.org/10.1029/2011wr011453

Lawrence, D. M., Fisher, R. A., Koven, C. D., Oleson, K. W., Swenson, S. C., Bonan, G., et al. (2019). The Community Land Model version 5: Description of new features, benchmarking, and impact of forcing uncertainty. *Journal of Advances in Modeling Earth Systems*, *11*(12), 4245–4287. https://doi.org/10.1029/2018ms001583

Lawrence, P. J., & Chase, T. N. (2007). Representing a new MODIS consistent land surface in the Community Land Model (CLM 3.0). *Journal of Geophysical Research*, *112*(G1), G01023. https://doi.org/10.1029/2006jg000168

Lee, T. J., & Pielke, R. A. (1992). Estimating the soil surface specific humidity. *Journal of Applied Meteorology and Climatology*, *31*(5), 480–484. https://doi.org/10.1175/1520-0450(1992)031<0480:etssh>2.0.co;2

Leung, L. R., Bader, D. C., Taylor, M. A., & McCoy, R. B. (2020). An introduction to the E3SM special collection: Goals, science drivers, development, and analysis. *Journal of Advances in Modeling Earth Systems*, *12*(11), e2019MS001821. https://doi.org/10.1029/2019ms001821

Li, H., Wigmosta, M. S., Wu, H., Huang, M., Ke, Y., Coleman, A. M., & Leung, L. R. (2013). A physically based runoff routing model for land surface and earth system models. *Journal of Hydrometeorology*, *14*(3), 808–828. https://doi.org/10.1175/jhm-d-12-015.1

Luo, L., Apps, D., Arcand, S., Xu, H., Pan, M., & Hoerling, M. (2017). Contribution of temperature and precipitation anomalies to the California drought during 2012–2015. *Geophysical Research Letters*, *44*(7), 3184–3192. https://doi.org/10.1002/2016gl072027

Ma, N., Niu, G. Y., Xia, Y., Cai, X., Zhang, Y., Ma, Y., & Fang, Y. (2017). A systematic evaluation of Noah-MP in simulating land-atmosphere energy, water, and carbon exchanges over the continental United States. *Journal of Geophysical Research: Atmospheres*, *122*(22), 12245–12268. https://doi.org/10.1002/2017jd027597

Maxwell, R., Chow, F. K., & Kollet, S. J. (2007). The groundwater–land-surface–atmosphere connection: Soil moisture effects on the atmospheric boundary layer in fully-coupled simulations. *Advances in Water Resources*, *30*(12), 2447–2466. https://doi.org/10.1016/j.advwatres.2007.05.018

Maxwell, R., & Condon, L. E. (2016). Connections between groundwater flow and transpiration partitioning. *Science*, *353*(6297), 377–380. https://doi.org/10.1126/science.aaf7891

Maxwell, R., & Kollet, S. J. (2008). Interdependence of groundwater dynamics and land-energy feedbacks under climate change. *Nature Geoscience*, *1*(10), 665–669. https://doi.org/10.1038/ngeo315

Maxwell, R. M., & Miller, N. L. (2005). Development of a coupled land surface and groundwater model. *Journal of Hydrometeorology*, *6*(3), 233–247. https://doi.org/10.1175/jhm422.1

Mohanty, B., Kanwar, R. S., & Everts, C. (1994). Comparison of saturated hydraulic conductivity measurement methods for a glacial-till soil. *Soil Science Society of America Journal*, *58*(3), 672–677. https://doi.org/10.2136/sssaj1994.03615995005800030006x

Newman, A. J., Clark, M. P., Winstral, A., Marks, D., & Seyfried, M. (2014). The use of similarity concepts to represent subgrid variability in land surface models: Case study in a snowmelt-dominated watershed. *Journal of Hydrometeorology*, *15*(5), 1717–1738. https://doi.org/10.1175/jhm-d-13-038.1

Nijssen, B., Lettenmaier, D. P., Liang, X., Wetzel, S. W., & Wood, E. F. (1997). Streamflow simulation for continental-scale river basins. *Water Resources Research*, *33*(4), 711–724. https://doi.org/10.1029/96wr03517

Niu, G. Y., Paniconi, C., Troch, P. A., Scott, R. L., Durcik, M., Zeng, X., et al. (2014). An integrated modelling framework of catchment-scale ecohydrological processes: 1. Model description and tests over an energy-limited watershed. *Ecohydrology*, *7*(2), 427–439. https://doi.org/10.1002/eco.1362

Niu, G.-Y., & Yang, Z.-L. (2006). Effects of frozen soil on snowmelt runoff and soil water storage at a continental scale. *Journal of Hydrometeorology*, *7*(5), 937–952. https://doi.org/10.1175/jhm538.1

Niu, G. Y., Yang, Z. L., Dickinson, R. E., & Gulden, L. E. (2005). A simple TOPMODEL-based runoff parameterization (SIMTOP) for use in global climate models. *Journal of Geophysical Research*, *110*(D21), D21106. https://doi.org/10.1029/2005jd006111

Nobre, A. D., Cuartas, L. A., Hodnett, M., Rennó, C. D., Rodrigues, G., Silveira, A., & Saleska, S. (2011). Height above the nearest drainage–a hydrologically relevant new terrain model. *Journal of Hydrology*, *404*(1–2), 13–29. https://doi.org/10.1016/j.jhydrol.2011.03.051

O'neill, M. M., Tijerina, D. T., Condon, L. E., & Maxwell, R. M. (2021). Assessment of the ParFlow–CLM CONUS 1.0 integrated hydrologic model: Evaluation of hyper-resolution water balance components across the contiguous United States. *Geoscientific Model Development*, *14*(12), 7223–7254. https://doi.org/10.5194/gmd-14-7223-2021

Paniconi, C., & Putti, M. (1994). A comparison of Picard and Newton iteration in the numerical solution of multidimensional variably saturated flow problems. *Water Resources Research*, *30*(12), 3357–3374. https://doi.org/10.1029/94wr02046

Paniconi, C., Troch, P. A., van Loon, E. E., & Hilberts, A. G. (2003). Hillslope-storage Boussinesq model for subsurface flow and variable source areas along complex hillslopes: 2. Intercomparison with a three-dimensional Richards equation model. *Water Resources Research*, *39*(11), 1317. https://doi.org/10.1029/2002wr001730

Paniconi, C., & Wood, E. F. (1993). A detailed model for simulation of catchment scale subsurface hydrologic processes. *Water Resources Research*, *29*(6), 1601–1620. https://doi.org/10.1029/92wr02333

Pelletier, J. D., Broxton, P. D., Hazenberg, P., Zeng, X., Troch, P. A., Niu, G. Y., et al. (2016). A gridded global data set of soil, intact regolith, and sedimentary deposit thicknesses for regional and global land surface modeling. *Journal of Advances in Modeling Earth Systems*, *8*(1), 41–65. https://doi.org/10.1002/2015ms000526

Pirastru, M., Iovino, M., Marrosu, R., Di Prima, S., Giadrossich, F., & Awada, H. (2022). Large-scale lateral saturated soil hydraulic conductivity as a metric for the connectivity of subsurface flow paths at hillslope scale. *Hydrological Processes*, *36*(8), e14649. https://doi.org/10.1002/hyp.14649

Qiu, H., Bisht, G., Li, L., Hao, D., & Xu, D. (2023). Development of inter-grid cell lateral unsaturated and saturated flow model in the E3SM land model (v2. 0). *EGUsphere*, *2023*, 1–31.

Sakaguchi, K., & Zeng, X. (2009). Effects of soil wetness, plant litter, and under-canopy atmospheric stability on ground evaporation in the Community Land Model (CLM3.5). *Journal of Geophysical Research*, *114*(D1), D01107. https://doi.org/10.1029/2008jd010834

Sakumura, C., Bettadpur, S., & Bruinsma, S. (2014). Ensemble prediction and intercomparison analysis of GRACE time-variable gravity field models. *Geophysical Research Letters*, *41*(5), 1389–1397. https://doi.org/10.1002/2013gl058632

Scanlon, B. R., Zhang, Z., Save, H., Sun, A. Y., Müller Schmied, H., Van Beek, L. P., et al. (2018). Global models underestimate large decadal declining and rising water storage trends relative to GRACE satellite data. *Proceedings of the National Academy of Sciences*, *115*(6), E1080–E1089. https://doi.org/10.1073/pnas.1704665115

Schaake, J. C., Koren, V. I., Duan, Q. Y., Mitchell, K., & Chen, F. (1996). Simple water balance model for estimating runoff at different spatial and temporal scales. *Journal of Geophysical Research*, *101*(D3), 7461–7475. https://doi.org/10.1029/95jd02892

Schubert, S. D., Suarez, M. J., Pegion, P. J., Koster, R. D., & Bacmeister, J. T. (2004). On the cause of the 1930s dust bowl. *Science*, *303*(5665), 1855–1859. https://doi.org/10.1126/science.1095048

Shen, C., Niu, J., & Phanikumar, M. S. (2013). Evaluating controls on coupled hydrologic and vegetation dynamics in a humid continental climate watershed using a subsurface-land surface processes model. *Water Resources Research*, *49*(5), 2552–2572. https://doi.org/10.1002/wrcr.20189

Shrestha, P., Sulis, M., Simmer, C., & Kollet, S. (2015). Impacts of grid resolution on surface energy fluxes simulated with an integrated surface-groundwater flow model. *Hydrology and Earth System Sciences*, *19*(10), 4317–4326. https://doi.org/10.5194/hess-19-4317-2015

Shrestha, P., Sulis, M., Simmer, C., & Kollet, S. (2018). Effects of horizontal grid resolution on evapotranspiration partitioning using TerrSysMP. *Journal of Hydrology*, *557*, 910–915. https://doi.org/10.1016/j.jhydrol.2018.01.024

Stieglitz, M., Rind, D., Famiglietti, J., & Rosenzweig, C. (1997). An efficient approach to modeling the topographic control of surface hydrology for regional and global climate modeling. *Journal of Climate*, *10*(1), 118–137. https://doi.org/10.1175/1520-0442(1997)010<0118:aeatmt>2.0.co;2

Subin, Z., Milly, P. C., Sulman, B., Malyshev, S., & Shevliakova, E. (2014). Resolving terrestrial ecosystem processes along a subgrid topographic gradient for an earth-system model. *Hydrology and Earth System Sciences Discussions*, *11*(7), 8443–8492.

Swenson, S., Clark, M., Fan, Y., Lawrence, D. M., & Perket, J. (2019). Representing intrahillslope lateral subsurface flow in the community land model. *Journal of Advances in Modeling Earth Systems*, *11*(12), 4044–4065. https://doi.org/10.1029/2019ms001833

Swenson, S. C., Lawrence, D. M., & Lee, H. (2012). Improved simulation of the terrestrial hydrological cycle in permafrost regions by the Community Land Model. *Journal of Advances in Modeling Earth Systems*, *4*(3), M08002. https://doi.org/10.1029/2012ms000165

Tai, X., Anderegg, W. R., Blanken, P. D., Burns, S. P., Christensen, L., & Brooks, P. D. (2020). Hillslope hydrology influences the spatial and temporal patterns of remotely sensed ecosystem productivity. *Water Resources Research*, *56*(11), e2020WR027630. https://doi.org/10.1029/2020wr027630

Tai, X., Venturas, M. D., Mackay, D. S., Brooks, P. D., & Flanagan, L. B. (2021). Lateral subsurface flow modulates forest mortality risk to future climate and elevated CO2. *Environmental Research Letters*, *16*(8), 084015. https://doi.org/10.1088/1748-9326/ac1135

Tesfa, T. K., Leung, L. R., & Ghan, S. J. (2020). Exploring topography-based methods for downscaling subgrid precipitation for use in Earth System Models. *Journal of Geophysical Research: Atmospheres*, *125*(5), e2019JD031456. https://doi.org/10.1029/2019jd031456

Tesfa, T. K., & Leung, L.-Y. R. (2017). Exploring new topography-based subgrid spatial structures for improving land surface modeling. *Geoscientific Model Development*, *10*(2), 873–888. https://doi.org/10.5194/gmd-10-873-2017

Tian, W., Li, X., Cheng, G.-D., Wang, X.-S., & Hu, B. (2012). Coupling a groundwater model with a land surface model to improve water and energy cycle simulation. *Hydrology and Earth System Sciences*, *16*(12), 4707–4723. https://doi.org/10.5194/hess-16-4707-2012

Ting, M., Seager, R., Li, C., Liu, H., & Henderson, N. (2018). Mechanism of future spring drying in the southwestern United States in CMIP5 models. *Journal of Climate*, *31*(11), 4265–4279. https://doi.org/10.1175/jcli-d-17-0574.1

Troch, P. A., Paniconi, C., & Emiel van Loon, E. (2003). Hillslope-storage Boussinesq model for subsurface flow and variable source areas along complex hillslopes: 1. Formulation and characteristic response. *Water Resources Research*, *39*(11), 1316. https://doi.org/10.1029/2002wr001728

Ullrich, P., Xu, Z., Rhoades, A., Dettinger, M., Mount, J., Jones, A., & Vahmani, P. (2018). California's drought of the future: A midcentury recreation for the exceptional conditions of 2012–2017. *Earth's Future*, *6*(11), 1568–1587. https://doi.org/10.1029/2018ef001007

Wang, Y., Mao, J., Jin, M., Hoffman, F. M., Shi, X., Wullschleger, S. D., & Dai, Y. (2021). Development of observation-based global multilayer soil moisture products for 1970 to 2016. *Earth System Science Data*, *13*(9), 4385–4405. https://doi.org/10.5194/essd-13-4385-2021

Warrach, K., Stieglitz, M., Mengelkamp, H.-T., & Raschke, E. (2002). Advantages of a topographically controlled runoff simulation in a soil–vegetation–atmosphere transfer model. *Journal of Hydrometeorology*, *3*(2), 131–148. https://doi.org/10.1175/1525-7541(2002)003<0131:aoatcr>2.0.co;2

Wigmosta, M. S., Vail, L. W., & Lettenmaier, D. P. (1994). A distributed hydrology-vegetation model for complex terrain. *Water Resources Research*, *30*(6), 1665–1679. https://doi.org/10.1029/94wr00436

Williams, A. P., Cook, E. R., Smerdon, J. E., Cook, B. I., Abatzoglou, J. T., Bolles, K., et al. (2020). Large contribution from anthropogenic warming to an emerging North American megadrought. *Science*, *368*(6488), 314–318. https://doi.org/10.1126/science.aaz9600

Xia, Y., Mitchell, K., Ek, M., Sheffield, J., Cosgrove, B., Wood, E., et al. (2012). Continental-scale water and energy flux analysis and validation for the North American Land Data Assimilation System project phase 2 (NLDAS-2): 1. Intercomparison and application of model products. *Journal of Geophysical Research*, *117*(D3), D03109. https://doi.org/10.1029/2011jd016048

Xie, Z., Di, Z., Luo, Z., & Ma, Q. (2012). A quasi-three-dimensional variably saturated groundwater flow model for climate modeling. *Journal of Hydrometeorology*, *13*(1), 27–46. https://doi.org/10.1175/jhm-d-10-05019.1

Xue, Y., & Shukla, J. (1993). The influence of land surface properties on Sahel climate. Part 1: Desertification. *Journal of Climate*, *6*(12), 2232–2245. https://doi.org/10.1175/1520-0442(1993)006<2232:tiolsp>2.0.co;2

Yang, Z.-L., & Dickinson, R. E. (1996). Description of the biosphere-atmosphere transfer scheme (BATS) for the soil moisture workshop and evaluation of its performance. *Global and Planetary Change*, *13*(1–4), 117–134. https://doi.org/10.1016/0921-8181(95)00041-0

Yang, Z.-L., & Niu, G.-Y. (2003). The versatile integrator of surface and atmosphere processes: Part 1. Model description. *Global and Planetary Change*, *38*(1–2), 175–189. https://doi.org/10.1016/s0921-8181(03)00028-6

York, J. P., Person, M., Gutowski, W. J., & Winter, T. C. (2002). Putting aquifers into atmospheric simulation models: An example from the Mill Creek Watershed, northeastern Kansas. *Advances in Water Resources*, *25*(2), 221–238. https://doi.org/10.1016/s0309-1708(01)00021-5

Youngs, E. (1987). Estimating hydraulic conductivity values from ring infiltrometer measurements. *Journal of Soil Science*, *38*(4), 623–632. https://doi.org/10.1111/j.1365-2389.1987.tb02159.x

Zeng, X., Broxton, P., & Dawson, N. (2018). Snowpack change from 1982 to 2016 over conterminous United States. *Geophysical Research Letters*, *45*(23), 12940–12947. https://doi.org/10.1029/2018gl079621

Zeng, X., & Decker, M. (2009). Improving the numerical solution of soil moisture–based Richards equation for land models with a deep or shallow water table. *Journal of Hydrometeorology*, *10*(1), 308–319. https://doi.org/10.1175/2008jhm1011.1

Zeng, Y., Xie, Z., Liu, S., Xie, J., Jia, B., Qin, P., & Gao, J. (2018). Global land surface modeling including lateral groundwater flow. *Journal of Advances in Modeling Earth Systems*, *10*(8), 1882–1900. https://doi.org/10.1029/2018ms001304

Zeng, Y., Xie, Z., Yu, Y., Liu, S., Wang, L., Zou, J., et al. (2016). Effects of anthropogenic water regulation and groundwater lateral flow on land processes. *Journal of Advances in Modeling Earth Systems*, *8*(3), 1106–1131. https://doi.org/10.1002/2016ms000646

Zhang, X. Y., Jin, J., Zeng, X., Hawkins, C. P., Neto, A. A., & Niu, G. Y. (2022). The compensatory CO2 fertilization and stomatal closure effects on runoff projection from 2016–2099 in the western United States. *Water Resources Research*, *58*(1), e2021WR030046. https://doi.org/10.1029/2021wr030046

Zhao, M., Liu, Y., & Konings, A. G. (2022). Evapotranspiration frequently increases during droughts. *Nature Climate Change*, 1–7.